Temporal variability and tidal modulation of hydrothermal exit–fluid temperatures at the Lucky Strike deep–sea vent field, Mid–Atlantic Ridge,

Thibault Barreyre, Javier Escartin, Rob Sohn, Mathilde Cannat, Valérie Ballu, Wayne Crawford

AGU PUBLICATIONS

JGR

Journal of Geophysical Research: Solid Earth

RESEARCH ARTICLE
10.1002/2013JB010478

Key Points:
- High-temperature outflow at deep-sea vent dominated by tidal pressure
- Lucky Strike displays stability in temperature over three years of monitoring
- Episodic temperature perturbations are local and shallow

Correspondence to:
T. Barreyre,
tbarreyre@whoi.edu

Citation:
Barreyre, T., J. Escartín, R. A. Sohn, M. Cannat, V. Ballu, and W. C. Crawford (2014), Temporal variability and tidal modulation of hydrothermal exit-fluid temperatures at the Lucky Strike deep-sea vent field, Mid-Atlantic Ridge, *J. Geophys. Res. Solid Earth*, *119*, 2543–2566, doi:10.1002/2013JB010478.

Received 1 JUL 2013
Accepted 9 FEB 2014
Accepted article online 15 FEB 2014
Published online 2 APR 2014

Temporal variability and tidal modulation of hydrothermal exit-fluid temperatures at the Lucky Strike deep-sea vent field, Mid-Atlantic Ridge

Thibaut Barreyre[1,2], Javier Escartín[1], Robert A. Sohn[2], Mathilde Cannat[1], Valérie Ballu[3], and Wayne C. Crawford[1,3]

[1]Marine Geosciences Group, Institut de Physique du Globe de Paris, CNRS, UMR 7154, Univ. Paris Diderot, Sorbonne Paris Cité, Paris Cedex 5, France, [2]Woods Hole Oceanographic Institution, Woods Hole, Massachusetts, USA, [3]LIENSs, Université de La Rochelle, CNRS, UMR 7266, La Rochelle, France

Abstract We deployed autonomous temperature sensors at black smoker chimneys, cracks, and diffuse flow areas at the Lucky Strike hydrothermal field (Mid-Atlantic Ridge, ~37°17′N) between summer 2009 and summer 2012 and contemporaneously measured tidal pressures and currents as part of the long-term MoMAR experiment to monitor hydrothermal activity. We classify the temperature data according to the hydrogeologic setting of the measurement sites: a high-temperature regime (>190°C) representing discharge of essentially unmixed, primary hydrothermal fluids through chimneys, an intermediate-temperature regime (10–100°C) associated with mixing of primary fluids with cold pore fluids discharging through cracks, and a low-temperature regime (<10°C) associated with a thermal boundary layer forming over bacterial mats associated with diffuse outflow of warm fluids. Temperature records from all the regimes exhibit variations at semi-diurnal tidal periods, and cross-spectral analyses reveal that high-temperature discharge correlates to tidal pressure while low-temperature discharge correlates to tidal currents. Intermediate-temperature discharge exhibits a transitional behavior correlating to both tidal pressure and currents. Episodic perturbations, with transient temperature drops of up to ~150°C, which occur in the high-temperature and intermediate-temperature records, are not observed on multiple probes (including nearby probes at the same site), and they are not correlated with microearthquake activity, indicating that the perturbation mechanism is highly localized at the measurement sites within the hydrothermal structures. The average temperature at a given site may increase or decrease at annual time scales, but the average temperature of the hydrothermal field, as a whole, appears to be stable over our 3 year observation period.

1. Introduction

The space-time variability of exit-fluid temperatures measured at deep-sea vent fields provides important information regarding the hydrogeology and subsurface circulation patterns of hydrothermal flow in young oceanic crust. This is critical for understanding the fluid-dynamical interaction between vents and the overlying ocean and to constrain associated heat, mass, and chemical fluxes. For modeling purposes, hydrothermal systems are often conceptualized as steady-state flow environments [e.g., *Lister*, 1980; *Cann and Strens*, 1989; *Sleep*, 1991] or as varying [*Lowell and Burnell*, 1991; *Fontaine et al*., 2008; *Han et al*., 2013] over longer time scales than those of the field observations (e.g., discharge rates and temperatures), which also exhibit significant spatial variability [e.g. *Fornari et al*., 1998; *Lilley et al*., 2003; *Scheirer et al*., 2006; *Sohn*, 2007a; *Larson et al*., 2007, 2009].

Time series temperature measurements made at mid-ocean ridge hydrothermal vents have demonstrated two distinct modes of temporal variability: episodic responses to perturbations from tectonic, magmatic, or mineralization processes [e.g., *Sohn et al*., 1998; *Johnson et al*., 2000; *Sohn*, 2007b; *Gribbin et al*., 2012] and periodic oscillations related to tidal processes [e.g., *Kinoshita et al*., 1998; *Davis and Becker*, 1999; *Tivey et al*., 2002; *Jupp and Schultz*, 2004; *Crone and Wilcock*, 2005; *Scheirer et al*., 2006; *Sohn*, 2007a].

Crustal permeability and vertical flow velocity, which are difficult to measure in the field, are fundamental parameters of the hydrothermal system [e.g., *Wilcock and McNabb*, 1996; *Jupp and Schultz*, 2004; *Crone and Wilcock*, 2005] and may be constrained from the response of the system to external forcing. On this point,

however, progress has been limited by the paucity of deep-sea vent exit-fluid data and uncertainties over the nature of the perturbation processes [e.g., *Lowell and Germanovich*, 1994; *Germanovich et al*., 2000, 2001; *Ramondenc et al*., 2006].

The existing data also demonstrated that there are broadly two types of hydrothermal venting: focused, high-temperature discharge from chimney structures (>100°C and often between 300°C and up to ~400°C) and diffuse, low-temperature (<100°C) discharge from cracks, through the seafloor, or at mineral deposits [*Corliss et al*., 1979]. Temperature measurements from sites of focused flow can be remarkably stable over time periods of up to a few years [*Langmuir et al*., 1997; *Fornari et al*., 1998; *Scheirer et al*., 2006; *Larson et al*., 2007, 2009], whereas temperature measurements from diffuse flow are much variable [*Tivey et al*., 2002; *Scheirer et al*., 2006; *Sohn*, 2007a]. This difference may result from the two types of discharge being associated with different circulation systems: focused flow and venting being associated with primary (deep) circulation and diffuse venting being associated with either secondary (shallow) circulation or leaking and mixing of primary fluids. Up until now, however, there have not been enough observatory-style measurements to determine if and how geological factors (e.g., ridge spreading rate, spreading modality, substrate type) and hydrogeological differences impact the nature of hydrothermal discharge.

Long-term (up to several years) temperature measurements have only been carried out at a few, geologically distinct mid-ocean ridge hydrothermal fields: the fast-spreading and volcanically active East Pacific Rise (EPR) at 9°50′N [*Fornari et al*., 1998; *Sohn et al*., 1998; *Scheirer et al*., 2006], the slow-spreading, detachment fault environment of the TAG segment of the Mid-Atlantic Ridge (MAR) [*Sohn*, 2007a], and the intermediate-spreading Cleft Segment [*Tivey et al*., 2002] and Main Endeavour Field (MEF) [*Larson et al*., 2007, 2009] along the Juan de Fuca Ridge (JdFR). Exit-fluid temperature records from all of these experiments have spatially complex episodic variability that is attributed to local geological or hydrogeological processes, and periodic variability at tidal frequencies (which could be caused by the tides themselves or tidally induced currents).

All long-term (on the order of a year or more) exit-fluid records from diffuse discharge sites exhibit some degree of periodic variability at tidal frequencies, but the details vary among sites. While poroelastic models predict tidal modulation of discharge velocity and temperature via the propagation of pressure transients into the shallow crust [e.g., *Jupp and Schultz*, 2004; *Crone and Wilcock*, 2005], discharge temperatures may also be affected by tidal and inertial bottom currents [JdFR, *Tivey et al*., 2002; MAR, *Kinoshita et al*., 1998]. Poroelastic theory predicts that periodic variability at tidal periods should be observed at sites of focused discharge, but, to date, this effect has only been reported at the MEF along the intermediate-spreading JdFR [*Larson et al*., 2007, 2009]. Exit-fluid temperature variations at tidal periods were observed over an approximately 2 month observation period for some of the focused discharge sites at the MEF, which were interpreted as resulting from subsurface mixing between non-seawater end-member fluids at, or just beneath, the interface between crustal layers 2A and 2B (i.e., 550 m under MEF [*Van Ark et al*., 2007]).

Here we report results from a 3 year field program to measure exit-fluid temperatures at nine sites from the Lucky Strike hydrothermal field on the slow-spreading MAR. This experiment benefits from contemporaneous measurements of exit-fluid temperature, bottom pressure, bottom currents, and local seismicity. First, these time series allow us to investigate the nature of temporal variability at sites of focused and diffuse outflow and to consider the hydrogeological implications for deep-sea vent fields and their interaction with the overlying water column. We apply a spectral analysis to objectively determine whether periodic variations of temperature records are forced by tidal currents or pressure. Second, these temperature records provide information regarding discharge stability at individual vent sites and at the scale of the hydrothermal field as a whole, over a time period of 3 years. Our analysis allows us to refine the hydrothermal discharge model for the Lucky Strike hydrothermal field, with implications for other basalt-hosted hydrothermal systems within the rift valley of slow-spreading ridge segments.

2. The Lucky Strike Hydrothermal Field

The Lucky Strike hydrothermal field (LSHF) is located at the summit of a central volcano on the ~80 km long Lucky Strike ridge segment, which extends along the MAR between 37°03′N and 37°37′N (Figure 1a). The central volcano is underlain at 3–4 km depth by an axial magma chamber (AMC) [*Singh et al*., 2006; *Combier*, 2007], which is the presumed heat source driving hydrothermal circulation at the LSHF. The southeastern vents have significantly lower Cl/Mg and higher $^{86}Sr/^{87}Sr$ than the northeastern and western vents

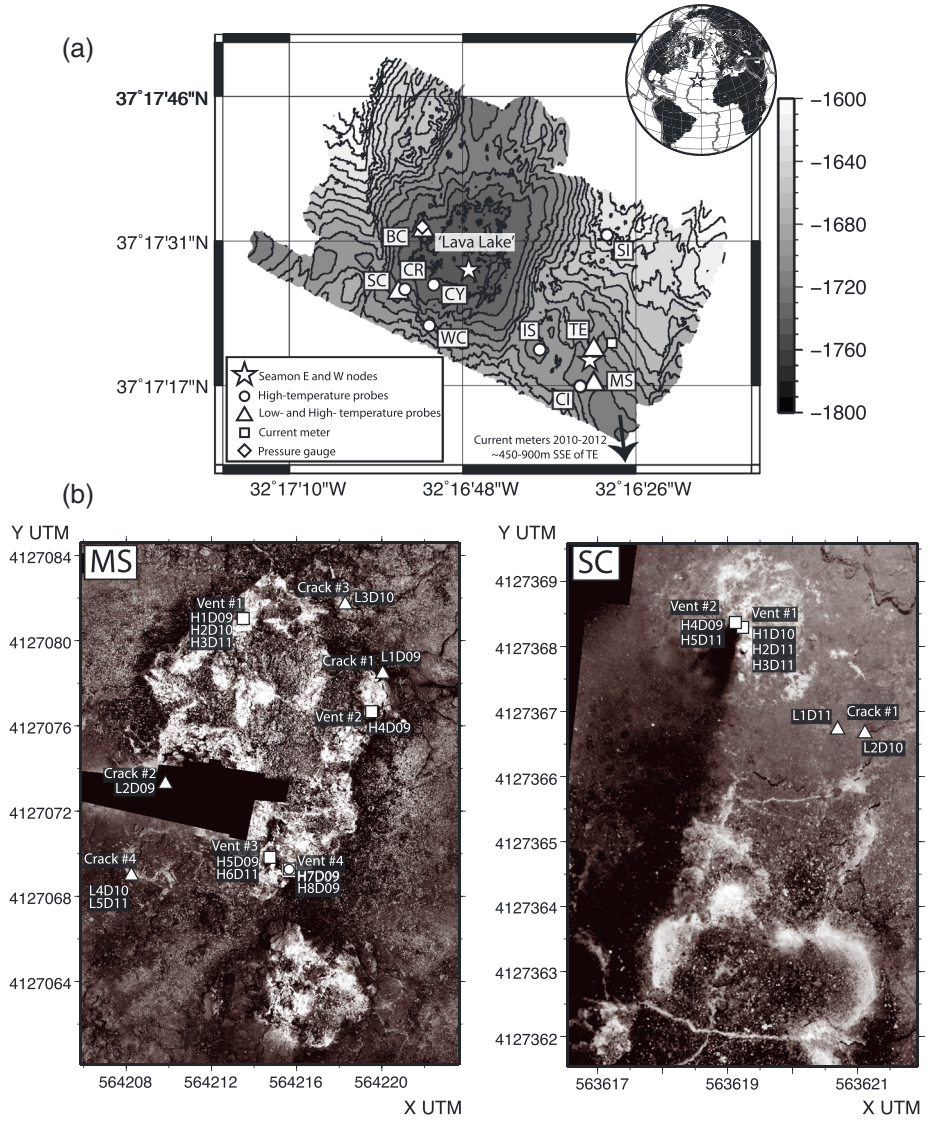

Figure 1. (a) Location of the main hydrothermal sites (boxed labels) at the Lucky Strike Hydrothermal Field (LSHF), and position of different geophysical instruments installed during Bathyluck'09, MoMARSAT10, MoMARSAT11 cruises: high-temperature probes (circles), high-temperature probes associated with low-temperature probes (triangles), the two MoMAR observatory nodes SEAMON E and W (stars), the pressure gauge (diamond), and the current meter 2009–2010 (square). Names of sites: TE: Tour Eiffel, MS: Montsegur, CI: Cimendef, IS: Isabel, SI: Sintra, WC: White Castle, CY: Cypress, BC: Benchmark C, CR: Crystal, and SC: South Crystal. The contour interval is 10 m. Multibeam bathymetry data from *Ondréas et al.* [2009]. (b) Photomosaics of the Montsegur (MS, left) and South Crystal (SC, right) sites, and location of temperature sensors. High-temperature probes are indicated by a white square (1 year probe recording) or a white circle (cruise-long probe recording). Low-temperature probes are indicated by a white triangle. Hydrothermal outflow is indicated by white areas (bacterial mats), which allow us to ascertain the geometry of fluid exit. *X* and *Y* axes are in Universal Transverse Mercator (UTM, meters). Resolution of photomosaic is up to 5 mm/pixel. Photomosaics from *Barreyre et al.* [2012]. Names of probes are shown "shorter" on the figure for better visibility; H is for high temperature (L for low temperature), and DXX gives year of the deployment. Sensor names corresponding to those reported in Table 2 are as follows. MS: H1D09: HW0007D09, H2D10: HW0014D10, H3D11: HW0020D11, H4D09: HW0009D09, H5D09: HN29007D09, H6D11: HN29014D11, H7D09: HN29013D09, H8D09: HN29014D09, L1D09: LW0004D09, L2D09: LW0001D09, L3D10: LW0005D10, L4D10: LW0002D10, L5D11: LW0015D11. SC: H1D10: HW0006D10, H2D11: HW0018D11, H3D11: HW0005D11, H4D09: HN29010D09, H5D11: HN30008D11, L1D11: LW0014D11, L2D10: LW0004D10.

[*Charlou et al.*, 2000], which could result from either two chemically distinct hydrothermal cells or phase separation of a similar source fluid [*Pester et al.*, 2012]. Microearthquakes at LSHF, interpreted to have a hydrothermal origin, suggest that the maximum depth of fluid penetration is ~3 km below the rift valley immediately north of the hydrothermal field, and somewhat shallower (~2.5km) immediately to the south [*Crawford et al.*, 2013].

Table 1. Summary of Autonomous Temperature Probe Deployments at Each Site for the 3 Years of Monitoring

	Deployment Period			
Site[a]	2009–2010	2010–2011	2011–2012	Total Monitoring Length
MS	5 HT 3 LT[b]	1 HT 2 LT	2 HT 1 LT	3 years
TE	4 HT 3 LT	3 LT[b]	1 HT 1 LT	3 years
CI	—	—	1 HT	1 year
IS	1 HT	—	1 HT	2 years
SI	2 HT	—	2 HT	2 years
CR	3 HT	1 HT	1 HT	3 years
SC	1 HT	1 HT 1 LT	3 HT 1 LT	3 years
CY	—	2 HT 1 LT[b]	1 HT	2 years
WC	3 HT	—	1 HT	2 years
BC	1 LT		—	2 years

[a]Location and names of sites are given in Figure 1 and Table 2, and geological settings and characteristics of the sites are given in section 2.
[b]LT sensors include one Starmon probe installed with a colonizer on bacterial mats.

The LSHF hosts several active hydrothermal sulfide structures, extending over an area of ~1 km^2 and surrounding a lava-filled depression 1740 m beneath the sea surface, often referred to as the "lava lake" (Figure 1a) [*Fouquet et al.*, 1995; *Ondréas et al.*, 2009; *Humphris et al.*, 2002; *Barreyre et al.*, 2012]. Extensive video imagery and seafloor image mosaics have revealed that hydrothermal discharge occurs through chimneys, mounds, and surrounding areas of diffuse outflow (i.e., patches, cracks) [*Barreyre et al.*, 2012]. Based on the videographic and photomosaic data, the total heat flux associated with the LSHF is estimated to be between ~200 and 1000 MW, with the major fraction on the east side of the field, primarily through diffuse flow [*Barreyre et al.*, 2012].

Throughout the LSHF, discharge tends to localize into discrete areas of both diffuse and focused flow. Image mosaics have been used to constrain the spatial limits of each site [*Barreyre et al.*, 2012; *Mittelstaedt et al.*, 2012]. The discharge zones are often located along fault scarps and fractures associated with the ~1 km wide axial graben that dissects the volcano. In this experiment, we instrumented nine hydrothermally active sites between 2009 and 2012 and obtained complete temporal coverage for four sites and partial coverage for the other five. Below we provide a brief description of each study site and the instrumentation strategy (Figure 1a and Table 1).

2.1. Montsegur (MS)

It extends over a 24 m × 16 m area in the SE of the LSHF and features two prominent sulfide mounds. The larger mound, in the north, is 10 m × 15 m and rises >5 m above the adjacent seafloor. The smaller mound, to the south, is 5 m × 6 m and rises ~3–4 m above the seafloor. Both are conical and are emplaced on a flat hydrothermal slab [*Langmuir et al.*, 1997; *Cooper et al.*, 2000; *Humphris et al.*, 2002; *Ondréas et al.*, 2009; and *Barreyre et al.*, 2012] composed of consolidated volcaniclastic material and hydrothermal minerals [*Gribbin et al.*, 2012]. We identified at least seven high-temperature vents in addition to extensive diffuse low-temperature discharge through cracks and the mounds flanks. This site was continuously monitored for outflow temperatures between 2009 and 2012.

2.2. Tour Eiffel (TE)

Located in the SE of the LSHF, it extends over a 24 m × 20 m area. A detailed description of this site and the heat fluxes associated with both diffused and localized flow is available in *Mittelstaedt et al.* [2012]. TE is dominated by a massive hydrothermal structure that rises ~20 m above surrounding seafloor [*Langmuir et al.*, 1997], located at the edge of a small fault scarp. Diffuse flow is mainly observed both on the walls of the edifice and around a crack network at the base of the hydrothermal structure. During our experiment, the hydrothermal edifice displayed at least eight clearly identified high-temperature vents, in addition to widespread diffuse flow through its surface and cracks. We continuously monitored this site for outflow temperatures between 2009 and 2012.

2.3. Cimendef (CI)

Located ~30 m west of Montsegur in the SE part of the LSHF, this site is emplaced on a hydrothermal slab and covers an area ~5 m in diameter. We identified only one small active chimney (~1 m high) and an associated

high-temperature vent, in addition to extensive diffuse flow and cracks around the structure. We monitored this site for outflow temperatures in 2011–2012.

2.4. Isabel (IS)

Located ~160 m west of Tour Eiffel in the SE part of the LSHF, this site covers an area ~5 m wide × 8 m long. We identified two small active chimneys (<1 m high) at the base of the edifice and three associated high-temperature vents, in addition to diffuse flow on the flank of the edifice, which is emplaced on hydrothermal slab. We monitored this site for outflow temperatures in 2009–2010 and in 2011–2012.

2.5. Sintra (SI)

This is a massive sulfide complex located in the north of the LSHF extending over an area ~7 m wide × ~5 m high [*Langmuir et al*., 1997]. High-temperature discharge mainly occurs along the top of a ridge formed by the complex. We identified at least four high-temperature vents, in addition to pervasive diffuse flow through most of the edifice's surface, which is largely covered by mussel beds. The high-temperature vent Sintra is the only active site in this NNE area of LSHF, and visual inspections suggest that it may be waning (observations from the yearly 2009 through 2012 cruises). We monitored outflow temperatures at this site in 2009–2010 and 2011–2012.

2.6. Crystal (CR)

Located in the west of the LSHF, this site extends over an area ~5 m in diameter. We identified at least three high-temperature vents on two parallel ridges, in addition to limited diffuse flow on these two ridges [*Von Damm et al*., 1998; *Humphris et al*., 2002]. A zone of remobilized hydrothermal deposits is located in between the ridges (observations from the yearly 2009 through 2012 cruises). We continuously monitored outflow temperatures from 2009 to 2012.

2.7. South Crystal (SC)

A ~2 m high conical hydrothermal complex located ~25 m SW of Crystal in the west part of the LSHF, it covers an area ~2 m diameter. We identified two high-temperature vents, in addition to an extensive diffuse flow zone and crack network about 7 m south of the mound (observations from the yearly 2009 through 2012 cruises). We continuously monitored outflow temperatures from 2009 to 2012.

2.8. Cypress (CY)

Located in the SW border of the lava lake in the central part of the LSHF, this site extends over an area ~5 m wide × ~10 m long. It includes a diffuse flow zone and several small (<1 m) high-temperature chimney structures. We identified at least three high-temperature vents, in addition to an extensive diffuse flow (observations from the yearly 2009 through 2012 cruises). We continuously monitored outflow temperatures from 2010 to 2012.

2.9. White Castle (WC)

Located in the SW part of the LSHF, this site extends over an area of 5 m × 6 m. We identified four high-temperature vents on the main active ridge, in addition to limited diffuse flow on both flanks, which are mainly composed of remobilized hydrothermal deposits (observations from the yearly 2009 through 2012 cruises). We monitored outflow temperatures between 2009–2010 and 2011–2012.

2.10. Benchmark C (BC)

This site corresponds to the ENE border of the lava lake, where a pressure gauge is installed over a benchmark. Temperature is measured in association with a geomicrobiological colonizator. There are no bacterial mats associated with hydrothermal activity at this site, and these data are used as a reference.

3. Instrumentation, Deployment Strategy, and Data Records

3.1. Instrumentation for Temperature Monitoring

We used four sets of instruments to monitor hydrothermal outflow temperature throughout the LSHF: MISO high-temperature probes, MISO low-temperature probes, NKE S2T6000 probes, and Starmon probes (Figure 2). The instrument-independent consistency of temperature measurements (i.e., repeatability) was assured by both factory and laboratory calibrations.

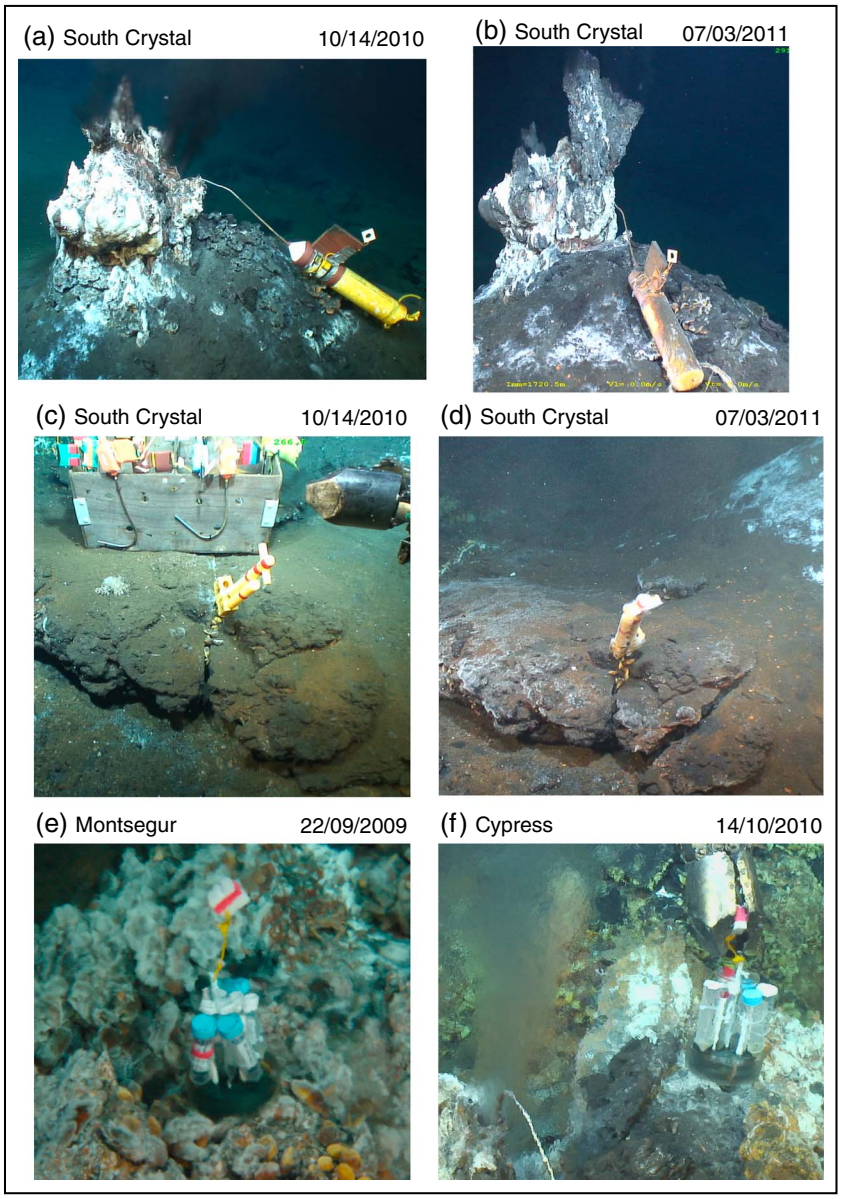

Figure 2. ROV dive video frames of probes deployed in 2010 (MoMARSAT10, left) and recovered in 2011 (MoMARSAT11, right) for Figures 2a–2d. (a) Example of high-temperature Woods Hole MISO probe deployment in black smoker at the South Crystal sulfide mound. (b) Video frame of the recovery of this high-temperature probe. Note that the vent orifice where HT probe was installed in 2010 has grown a 1 m chimney while probe is still recording fluid temperatures (see record in Figure 3). (c) Example of low-temperature Woods Hole probe deployment in diffuse crack hosted by South Crystal crack network. (d) Video frame of the recovery of this low-temperature probe. Note that the LT probe is still at the same place as in 2010 during its deployment. (e) Example of a low-temperature Starmon probe (associated to a colonizer) deployment on diffuse outflow at the Montsegur site in 2009. (f) Other example of a low-temperature Starmon probe (associated to a colonizer) deployment on diffuse outflow at the Cypress site in 2010. In Figures 2c, 2d, 2e, and 2f, white bacterial mats and mussels are visible in 2010 and are still present in 2011, indicating continuous outflow through a crack (c and d), and diffuse flow through the seafloor and bacterial mat (e and f), as indicated by the corresponding temperature records (Figure 3).

WHOI MISO high-temperature probes (HW) consist of a titanium body (~10 cm diameter × ~20 cm long), equipped with a ~75 cm-long titanium (Ti) rod. The housing hosts two Omega data loggers connected to a J-Type thermocouple located at the rod tip [*Fornari et al.*, 1994, 1996, 1998]. These instruments can record temperatures of up to 450°C with a precision and resolution of ±1.1°C and 0.21°C, respectively. The sampling interval was typically 24 min for our yearlong records. Each probe contained two loggers for redundancy, with the sampling times offset by 12 min to provide complementary temperature records (see Table 2).

AGU Journal of Geophysical Research: Solid Earth

10.1002/2013JB010478

Table 2. Summary of Temperature Records Used in This Study, Deployment Details, Average Temperature, and Trends[a]

Sites	Location XUTM/YUTM (m)	Name of Vent/Crack	Temperature Record Name	Deployement Date (mm/dd/aa)	Record Length (days)	Sampling Interval (s)	MeanT (°C)	stdT (°C)	Trend (°C/yr)
MS	564214 / 4127075								
		V01	MS_V01_090906_101004_HW0007A*	6/9/2009	392.795	1440	312.353	1.384	0.96
			MS_V01_101010_110706_HW0014A*	10/10/2010	268.967	1440	310.885	2.195	6.09
			MS_V01_110706_120717_HW0020B*	6/7/2011	376.329	1440	312.300	2.309	7.34
		V02	MS_V02_090906_101004_HW0009A	6/9/2009	392.909	1440	299.972	1.500	−0.92
		V03	MS_V03_090922_101004_HN29007	09/22/09	106.394	90	310.188	2.604	−10.36
			MS_V03_110710_120717_HN29014*	10/7/2011	372.488	90	307.817	0.580	−1.24
		V04	MS_V04_090906_090922_HN29014	6/9/2009	16.324	10	316.835	0.508	
			MS_V04_090922_101004_HN29013	09/22/09	36.664	90	313.755	0.695	
		C01	MS_C01_090907_101004_LW00004*	7/9/2009	390.824	901	67.037	2.710	−5.77
		C02	MS_C02_090907_101004_LW00001*	7/9/2009	391.326	900	29.232	14.400	41.70
		C03	MS_C03_101011_110706_LW00005*	11/10/2010	268.450	1440	11.979	9.388	18.91
		C04	MS_C04_101011_110706_LW00002*	11/10/2010	268.333	1440	8.642	6.111	−2.02
			MS_C04_110710_120716_LW00015*	10/7/2011	293.171	1440	13.195	8.449	18.19
		INC	MS_INC_090922_101004_LS02883*	09/22/09	374.767	180	5.337	0.773	−0.13
TE	564216 / 4127184								
		V02	TE_V02_090905_101003_HW0010B	5/9/2009	277.674	1440	318.792	6.175	8.38
		V03	TE_V03_090906_090922_HN29006	6/9/2009	10.764	10	304.934	7.037	
		V04	TE_V04_090906_090922_HN29017	6/9/2009	16.680	10	312.368	0.671	
		AIS	TE_AIS_090923_101010_HN29016b	09/23/09	40.540	90	289.934	7.487	
			TE_AIS_110720_120716_HN30015	07/20/11	36.488	180	297.122	1.071	
		C01	TE_C01_090907_101003_LW00002	7/9/2009	390.701	900	16.753	13.939	−24.64
			TE_C01_101015_110702_LW00001*	10/15/10	259.853	1440	7.670	2.813	6.63
		C02	TE_C02_090907_101003_LW00003	7/9/2009	297.664	900	96.467	1.219	−4.17
			TE_C02_101011_110702_LW00003	11/10/2010	65.216	1440	83.067	10.139	
			TE_C02_110720_120716_LW00011*	07/20/11	361.471	1440	68.633	21.454	−59.37
		C03	TE_C03_090907_101003_LW00005*	7/9/2009	389.304	900	40.997	33.921	−64.68
		INC	TE_SEN_101010_110702_LN26004*	10/10/2010	264.817	180	5.177	0.340	−0.03
CI	564185 / 4127070								
		V01	CI_V01_110710_120716_HW0012A	10/7/2011	37.201	1440	308.814	1.948	
IS	564059 / 4127247								
		V01	IS_V01_090923_101004_HW0012B	3/9/2009	376.111	1440	297.611	3.574	0.31
		V01	IS_V02_110712_120718_HW0001A*	12/7/2011	371.745	1440	303.099	0.229	−0.20
SI	564263 / 4127529								
		V01	SI_V01_090906_101010_HW0002A*	6/9/2009	398.178	1440	207.982	1.155	1.90
			SI_V01_110704_120714_HW0009A*	4/7/2011	374.903	1440	205.215	1.483	2.65
		V02	SI_V02_090923_101010_HN29012b*	09/23/09	381.974	90	207.186	1.218	−0.49
		V03	SI_V03_110704_120713_HN30009*	4/7/2011	374.959	90	199.966	1.158	−1.63
CR	563640 / 4127384								
		V01	CR_V01_090907_101004_HW0006A*	7/9/2009	391.176	1440	331.429	0.548	1.14
			CR_V01_101014_110703_HW0010B	10/14/10	31.617	1440	317.910	2.833	
		V02	CR_V02_090907_090922_HN29012	7/9/2009	14.111	10	329.266	1.398	
			CR_V02_110703_120716_HW0019B*	3/7/2011	378.272	1440	331.492	0.906	−1.66
		V03	CR_V03_090907_101004_HW0008A*	7/9/2009	166.822	1440	323.971	2.647	−16.19
SC	563619 /4127368								
		V01	SC_V01_101014_110703_HW0006B*	10/14/10	261.733	1440	339.318	0.854	−3.19
			SC_V01_110703_110716_HW0018A	3/7/2011	12.433	1440	339.195	0.188	
			SC_V01_110716_120716_HW0005B*	07/16/11	365.977	1440	334.848	3.226	−5.95
		V02	SC_V02_090922_101010_HN29010*	09/22/09	383.197	90	330.375	0.401	−1.11
			SC_V02_110716_120718_HN30008	07/16/11	29.216	90	335.682	2.667	

Table 2. (continued)

Sites	Location XUTM/YUTM (m)	Name of Vent/Crack	Temperature Record Name	Deployement Date (mm/dd/aa)	Record Length (days)	Sampling Interval (s)	MeanT (°C)	stdT (°C)	Trend (°C/yr)
		C01	SC_C01_101014_110703_LW00004*	10/14/10	261.617	1440	14.806	1.238	−2.20
			SC_C01_110703_120716_LW00014*	3/7/2011	378.590	1440	13.606	0.865	−0.62
CY	563725 / 4127379								
		V01	CY_V01_101015_110703_HN30008*	10/15/10	129.014	180	292.873	0.977	−5.46
			CY_V01_110704_120716_HN30001*	4/7/2011	378.139	90	300.312	2.383	6.09
		V02	CY_V02_101014_110703_HN30010	10/14/10	73.625	180	291.048	2.721	
		INC	CY_INC_101014_110705_LN27010*	10/14/10	261.816	180	4.873	0.492	−0.40
WC	563717 / 4127255								
		V01	WC_V01_090915_101010_HW0004B	09/15/09	30.851	1440	316.110	0.834	
		V02	WC_V02_090908_090921_HN29002	8/9/2009	13.925	10	306.805	0.740	
			WC_V02_090921_110704_HN29020	09/21/09	43.763	90	309.458	0.867	
		V03	WC_V03_110704_120717_HN30003*	4/7/2011	379.477	90	311.834	0.237	−0.06
BC	563760 / 4127466								
		INC	BC_INC_090915_110701_LS02886*	09/15/09	653.519	180	4.237	0.078	−0.01

[a]The name of the record includes the initials of hydrothermal sites (see Figure 1), the date and time of deployment, the sensor type (LW, HW, HN, LN, LS), and serial number. Asterisk behind probe names denotes probes that were used for coherence calculation shown in Figure 11. Raw temperature records are publicly available as doi:10.1594/PANGAEA.820343.

WHOI MISO low-temperature minilog probes (LW) have a smaller Ti housing (~2.5 cm diameter × ~11 cm long) and a ~13 cm Ti rod. These instruments are equipped with a single data logger connected to a thermistor located at the rod tip. These low-temperature instruments can record temperatures of up to 125°C with a precision and a resolution of ±0.22°C and 0.025°C, respectively. The sampling frequency was set to 15 min for instruments deployed in 2009 and 24 min for those deployed in 2010–2011 (Table 2).

NKE S2T6000 high-temperature probes (HN) consist of a cylindrical Ti housing (12.8 cm length and 2.3 cm in diameter) and a 40 cm long rod. The data logger is connected to a P-T thermistor at the rod tip and can record temperatures ranging between 0°C and 450°C with a precision and a resolution of ±0.5°C (at less than 100°C) and 0.1°C, respectively. Sampling intervals were set at either 90 s or 3 min for the yearlong records, and at 10 s for the weeklong records (see Table 2).

Starmon low-temperature sensors (LS), which were designed to measure ambient bottom water temperature in the proximity of diffuse outflow, have a cylindrical (2.5 cm diameter × 10.8 cm long) Ti housing with a thermistor located at the tip of a 1.9 cm long rod. These sensors were installed within microbiological colonizers placed on bacterial mats. The probes are equipped with one data logger, recording temperature at a sampling rate of 3 min and over a temperature range of 0°C to 100°C with a precision and a resolution of ±0.05°C (at less than 40°C) and 0.013°C, respectively.

3.2. Bottom Pressure and Current Monitoring

The pressure and near-bottom current (speed and direction) were monitored during the deployment of the temperature sensors. A *Seabird* 53BPR pressure gauge was installed, as part of a larger seafloor geodesy experiment to monitor vertical deformation at Lucky Strike volcano [*Ballu et al.*, 2009], on the lava lake near the SEAMON-W EMSO (European Multidisciplinary Subsea Observatory) observatory node (Figure 1a). The site is near the foot of the western fault scarp bounding the axial graben. The sampling interval was 30 s for the entire observation period (2009–2012), and the accuracy and repeatability are, respectively, 0.01% and 0.005% of full scale (i.e., 4000 m).

A *NORTEK* Aquadopp current meter was deployed 14 m above the seafloor at a site ~60 m E of the TE site in 2009–2010, ~450 m SSE of the TE site in

2010–2011, and ~900 m SSE of the TE site in 2011–2012 (Figure 1a). Sampling intervals for the 3 years were set at 10, 3, and 6 min, respectively. Nominal velocity uncertainties are 1.4 cm/s in the vertical direction and 0.9 cm/s for the horizontal direction. Both pressure and current measurements instruments are serviced yearly for calibration.

3.3. Monitoring Strategy

We obtained exit-fluid time series data from 54 probes between September 2009 and July 2012, with record lengths varying from several weeks to about a year (Tables 1 and 2). Temperature sensors were deployed and recovered using the ROV *Victor* during annual cruises: Bathyluck'09, MoMARSAT'10, MoMARSAT'11, and MoMARSAT'12 (Figure 2). We targeted high-temperature vents ($>$190°C and up to ~350°C), cracks discharging lower-temperature, shimmering fluids ($<$100°C), and bacterial mats associated with low-temperature diffuse fluids (typically $<$10°C). Fifteen additional instruments were deployed but failed to return data because they were either burned by high-temperature fluids or lost due to chimney collapse or growth of hydrothermal deposits. Successful deployments yielding data and reported in Tables 1 and 2 are used in this study and represent a combined total of ~36.5 years of recording. Four sites (TE, MS, SC, CR) were instrumented for all 3 years of the monitoring experiment, five sites (IS, SI, CY, WC, BC) were instrumented for 2 years, and one site (CI) was instrumented for only the year 2011–2012 (see Table 1 for details). The raw temperature data are publicly available (doi:10.1594/PANGAEA.820343).

We conducted a nested monitoring approach in order to investigate variability across a spectrum of length scales (field scale, site to site, and site scale) and to provide redundancy in case of instrument failure or loss. At high-temperature vents, the HW and HN sensors were deployed with the sensor tip placed up to 10–15 cm inside the vent orifice in order to minimize variability associated with turbulent mixing of hydrothermal fluids with ambient seawater (Figures 2a and 2b). In lower temperature outflows, the tips of the LW sensors were placed within cracks discharging shimmering water (Figures 2c and 2d). At the microbial mat sites (TE, MS, BC, CY), the tips of the LS were placed in shimmering water at the surface of the mats (Figures 2e and 2f). Whenever possible, probes were redeployed in the same orifice or crack at each measurement site during the annual site visits (see Table 2 for details).

Instrument installation and temperature record interpretation are coupled with seafloor images derived from photomosaics [*Barreyre et al*., 2012; *Mittelstaedt et al*., 2012], allowing us to better understand the spatial relationships among temperature records, and with the overall fluid outflow throughout the site (Figure 1b). Seafloor imagery provides a complete view of actively venting areas, which allow us to determine the association of temperature records with specific venting structures to properly place our observations at the scale of the site, and to evaluate their representativeness.

3.4. Data Preprocessing and Time Series

The autonomous clocks for each probe were synchronized to GPS time before deployment and after recovery, and the timing of each temperature record was corrected assuming a linear drift. The average clock drift for HW probes was ~15 min over 1 year, which is comparable to one sampling interval. Each temperature record was visually inspected and trimmed to remove data acquired after the probe was dislodged from its deployment site. In most cases this corresponds to recovery by the ROV, but in some cases the probes became dislodged (e.g., fell out of the chimney or crack) prior to recovery, as verified by ROV video. A few probes became cemented within the wall of hydrothermal structures or chimneys, and these records display a gradual decay, likely associated with the migration of the hydrothermal conduit (i.e., flow) away from the probe tip. In such cases we terminated the record prior to the gradual decrease in temperature. In this paper we only present and analyze those portions of the temperature records that faithfully measured exit-fluid temperatures for a period of 10 days or more.

The bottom pressure and current-meter records were handled in a similar fashion to the exit-fluid records. The timing was corrected assuming a linear clock drift during the duration of deployments, and the records were inspected for spurious data. While the pressure sensor returned 3 years of continuous data (with yearly services), the current meter returned a complete record for the first year (2009–2010) and partial records (~110 days) for the second and third years of monitoring (2010–2011 and 2011–2012), due to data logging issues.

The ensemble set of the 54 temperature records, the bottom pressure record, and the current-meter data used in our analyses are shown in Figure 3. The number of temperature records available for a given time window varies depending on yearly instrumentation strategy, logistical deployment issues, loss of sensors, and truncation of records (see Table 2).

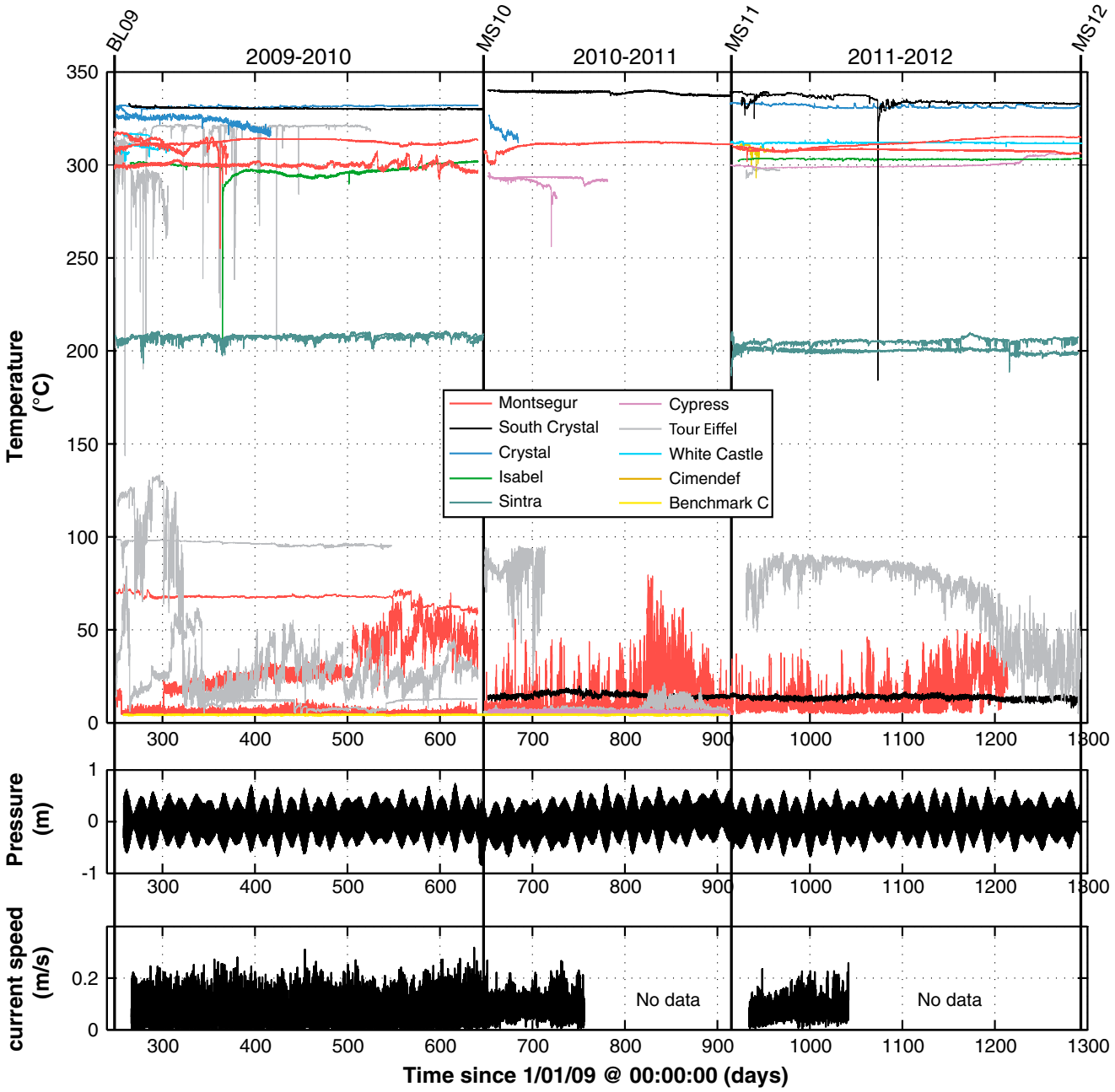

Figure 3. (Top) Plot showing all exit-fluid temperature records from the Lucky Strike hydrothermal field. Vertical lines correspond to the instrument recovery and deployments during cruises: Bathyluck09 (BL09), MoMARSAT10 (MS10), MoMARSAT11 (MS11), and MoMARSAT12 (MS12). (Middle) Pressure data for the monitoring period (conversion from dbars to meters is made using the matlab function sw_dpth, which is based on *Fofonoff and Millard Jr.* [1983] algorithms). (Bottom) Current-meter speed data for the same time window. The current meter failed between days ~775 and ~900 and between days ~1050 and ~1300.

4. Results

The temperature records we acquired from the LSHF can be divided into three categories corresponding to the average temperature and the hydrogeological setting (Figures 3 and 4): (1) High-temperature records acquired from chimneys of focused discharge display average temperatures >195°C; (2) Intermediate-temperature records acquired from cracks discharging shimmering fluids at average temperatures ranging between ~10°C and 100°C; and (3) Low-temperature records acquired from diffuse discharge zones populated by microbial mats, with average temperatures <10°C (Table 2 and Figures 4a and 4b).

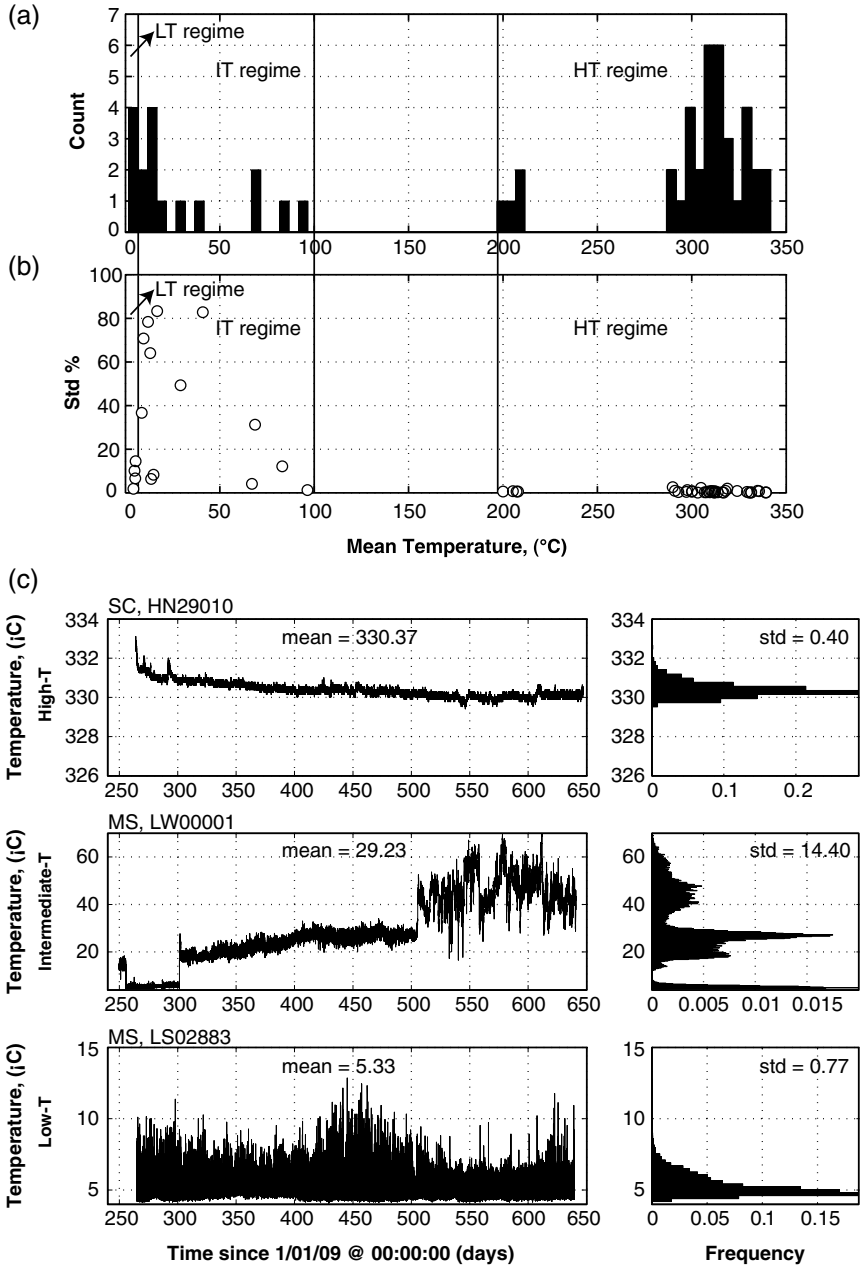

Figure 4. (a) Histogram of the mean of each of the 54 temperature records, defining the high-, intermediate-, and low-temperature regimes (HT, IT, and LT respectively). (b) Standard deviation normalized by the mean temperature in %, calculated for each record, plotted against mean temperature. (c) Examples of high-, medium-, and low- temperature records (top, middle, and bottom, respectively) and their corresponding histograms of temperature, with the frequency normalized by the total number of observations. The mean and standard deviation (std) for each temperature records is also indicated. Sites and names of the probes used as example are given on the top of each panel.

Figure 4c illustrates differences in behavior for selected temperature records in each of these three categories. High-temperature (HT) records are overall stable and display a low variability; one out of 22 high-temperature records longer than 100 days displays a standard deviation >4°C, while 14 display instead standard deviations of <2°C (<1% of the average temperature). These records typically exhibit unimodal temperature histograms with small (a few °C) deviations (Figure 4c). Intermediate-temperature (IT) records display more complex patterns, with higher standard deviations overall (with a maximum of >30°C), and episodic changes in discharge temperature. This is illustrated in Figure 4c (middle panel), where changes in both the average temperature and the standard deviation appear, yielding a multimodal histogram. Low-temperature (LT)

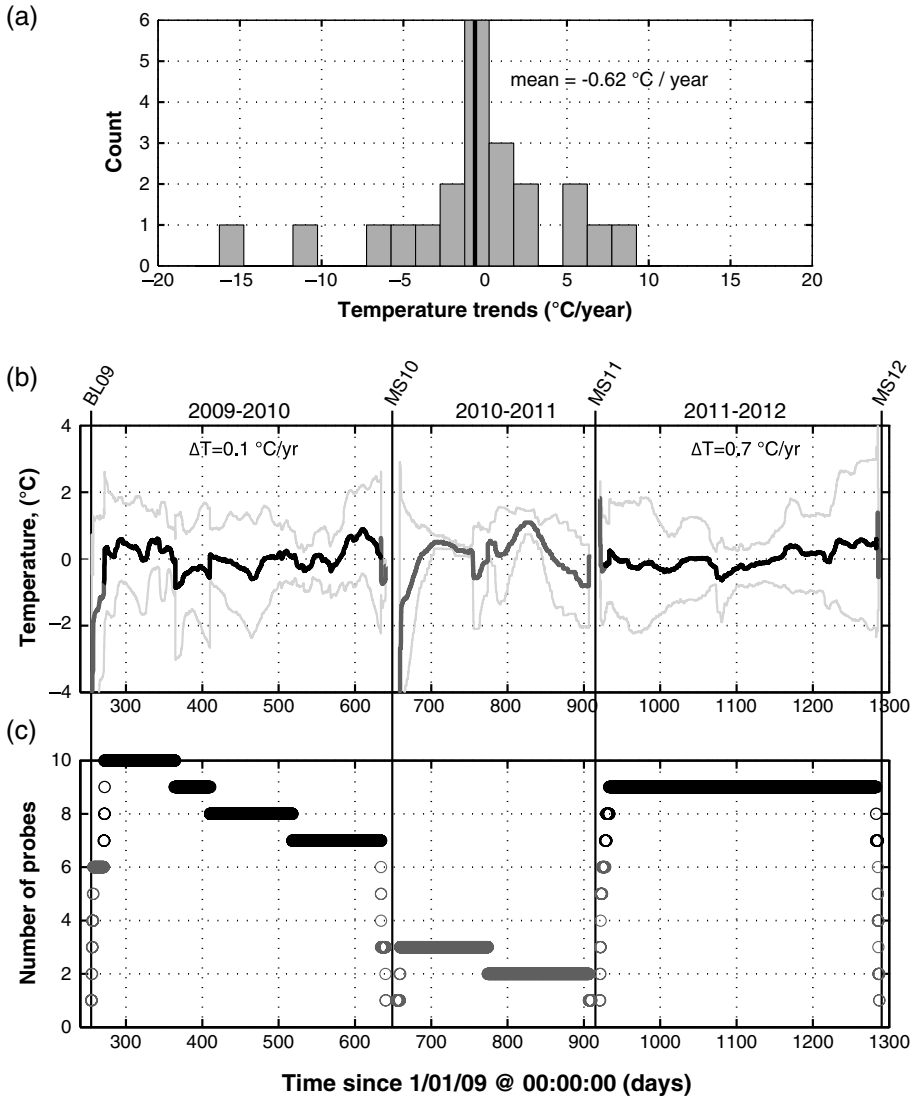

Figure 5. (a) Histogram of temperature trends calculated from high-temperature records spanning over 100 days or more. Vertical black line shows the mean value. (b) Composite average temperature for HT records longer than 100 days and corresponding standard deviation (thin light gray lines) for the 3 year monitoring period and (c) number of temperature records contributing to the composite temperature record. Only composite record sections calculated from six instruments or more, shown in black, are used to infer long-term temperature gradients, while the rest (thick dark gray line) are not considered.

records display average temperatures that are close to that of ambient seawater with low-amplitude (standard deviations of <1°C) continuous variability. While the absolute value of temperature deviations is lower than that observed for intermediate and high-temperature records, they represent up to 25% of the average temperature, compared to <3% for the high-temperature records. LT temperature histograms are unimodal and typically asymmetric (skewed to lower temperatures) (Figure 4c). As described below, these temperature records provide information on the temporal evolution of the LSHF at time scale of months to years (section 4.1) and both episodic and periodic variability on shorter time scales (sections 4.2 and 4.3, respectively).

4.1. Long-Term Evolution of Effluent Temperature

Table 2 reports the long-term temperature trends for all the records used in this study estimated using least squares linear regression. For the 38 records longer than 100 days, the annual trends vary between −65 and +41°C/yr, although most of them (20 out of 38) display trends less than 3°C/yr in magnitude. For the high-temperature records, the range in trends, shown in Figure 5a, is significantly reduced (−16 to +8°C/yr, 13 out 22 records with trends <3°C/yr in magnitude), with an average of −0.62°C/yr (Figure 5a and Table 2). We

Table 3. In Situ Measurements of High-Temperature Outflow at Selected Hydrothermal Vents (see *Ondréas et al.* [2009] and *Barreyre et al.* [2012] for Sites Locations) From the Lucky Strike Field (Temperatures in °C)[a]

	1993[b]	1994[c]	1996[d]	1997[e]	2008[fg]	2009[g]	2010[g]	2011[g]	2012[g]	Average ± Std[h]
Tour Eiffel	325	324	323	324	*184*[g]	317	*296*	325	322	322.8±2.8
Sintra	212	215	222	*176*	200[f]	196/217	–	209	203	211.1±7.8
Y3	333	324	328	–	319[f]	321	–	325	326	325.1±4.6
Statue of Liberty	202	185	–	–	–	Extinct				–
Crystal	–	–	*281*	–	–	327	327	335	–	329.7±4.6
M.7/Cimendef	302	310	–	306	–	–	–	308[CI]	–	306.5±3.4
South Crystal	–	–	–	–	–	340	–	342	340	340.7±1.1
White Castle	–	–	–	–	–	310	313	317	319	314.7±4.0
Isabel	–	*175*	–	–	–	–	–	305.6	304	304.8±1.1
Montsegur	303[i]	310[j]	318[j]	294[j]	–	296[k]	306[k]	316[k]	322[k]	308.1±10.2

[a]Numbers in italics correspond to values significantly lower than the average, and that we attribute to measurements within the mixing zone of seawater and hydrothermal fluids.
[b]FAZAR cruise [*Langmuir et al.*, 1997].
[c]DIVA 1 cruise [*Charlou et al.*, 2000].
[d]LUSTRE cruise [*Von Damm et al.*, 1998].
[e]Flores cruise [*Charlou et al.*, 2000; *Donval et al.*, 1997].
[f]KNOX18RR cruise (data from WHOI Deep Submergence database, JASON VirtualVan available at http://4dgeo.whoi.edu/jason/).
[g]This study, from cruises MoMAR (2008), Bathyluck (2009), MoMARSAT (2010, 2011, and 2012).
[h]Average and standard deviation do not include the temperatures in italics, which are considered anomalously low.
[i, j, k]: Sites at Montsegur: M6 (i), M4(j), and vents measured during MoMAR cruise, reported as Montsegur (k) and that may be distinct from M4 and M6, see *Barreyre et al.* [2012].

find that the magnitude and even the sign of the temperature trends can vary for records obtained from individual vent sites. For example, the temperature record acquired from vent #1 at Montsegur in 2009 exhibits a positive trend of 0.96°C/yr, whereas the record acquired from vent #2, located 6 m away (Figure 1b), exhibits a negative trend of −0.92°C/yr. Furthermore, vent #1 in Montsegur (Figure 1b, MS), displayed average temperatures and trends for each of the deployments of 312.35°C and 0.9°C/yr in 2009–2010, 310.88°C and 6°C/yr in 2010–2011, and 312.30°C and 7°C/yr in 2011–2012, respectively (Table 2).

Given the variability in long-term trends at individual sites and throughout the whole field, we have generated a composite temperature record at the scale of the LSHF for each of the deployments. We have selected the HT records from nine studied sites with durations of >100 days (Table 2). We have discarded intermediate- and low-temperature records, which exhibit complex patterns and changes in outflow regime (e.g., Figure 4c). To generate this composite record, we applied a 14 day running median filter to each record to remove short-term perturbations. We then removed the mean from each smoothed record. Finally, we average these resulting records to obtain a zero-mean composite temperature record and the corresponding standard deviation (Figure 5b). We note temporal variations in the number of sensors contributing to these composite records (Figure 5c), particularly during recovery and re-deployment. We consider that robust and meaningful estimates of temperature trends can only be obtained from composite records derived from six instruments or more (black line, Figure 5b, black circles, Figure 5c); the remaining records (thick dark gray line in Figures 5b and 5c) are not considered in this analysis. Note that some of the temporal variations of the composite record clearly correspond to changes in the number of instruments (e.g., temperature changes around days 360 and 410 in Figure 5a).

The trends obtained for 2009–2010 and 2011–2012 are 0.1 and 0.7°C/yr, and within the observed standard deviation of <2°C (Figure 5b). These values are comparable to the average of individual trends reported in Table 2, which yield −1.6 and 0.6°C/yr for 2009–2010 and 2010–2011 respectively. While it is not possible to derive a continuous composite record for the 3 years of monitoring, the average of trends from individual HT records is <1°C/yr (Figure 5a).

Temporal variability in temperature at longer time scales (up to two decades) can only be derived from historical, discrete temperature measurements from different sites throughout the LS hydrothermal field. The highest temperatures measured at any given year for each of the sites reported in the literature or measured during recent cruises to the LSHF are given in Table 3. We have excluded anomalously low values, with temperatures of several tens to more than a hundred degrees below historical values, and that we attribute to

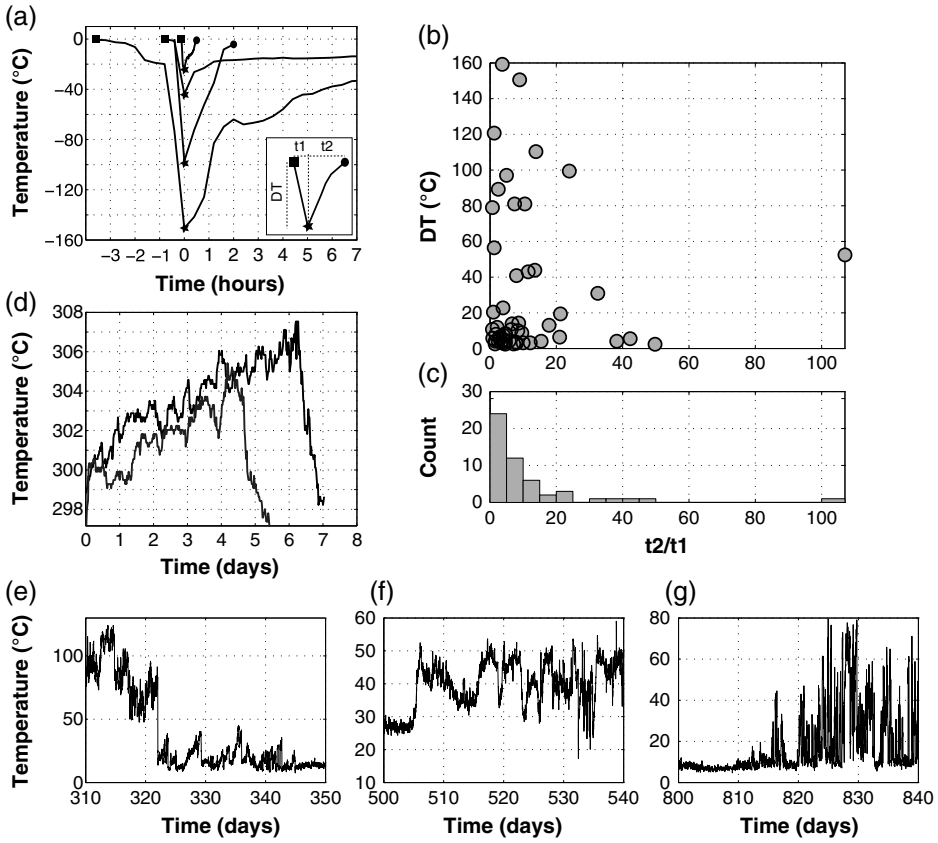

Figure 6. (a) Four selected examples of cooling events, with the *Y* axis showing the temperature minus the temperature (T_0) before the drop. (b) Plot showing the ratio between the time of recovery to the 95% of the temperature drop (t_2) and the time of the temperature drop (t_1) and the corresponding drop of temperature (DT). (c) Corresponding histogram of the ratio t_2/t_1. (d) The two warming events that have been observed in HT records. (e, f, g) Three different panels zooms corresponding to different examples of variability into IT records.

temperature measurements performed within the mixing zone and thus cooler than the high-temperature fluids. At sites monitored for ~20 years (TE, SIN, Y3, SL, CI, and MS), temperatures are very stable and display no apparent or significant decline or increase over time (trends in magnitude $<$1°C/yr). In the case of Montsegur (MS), this temporal evolution may not be well constrained, as there is ambiguity regarding sites of measurements (M4/U.S.4 and M6/U.S.6 vents, both at Montsegur mounds, see *Langmuir et al.* [1997]; *Von Damm et al.* [1998]; *Barreyre et al.* [2012]). For sites inspected since 2009 and with temperature measurements in the same vent (SC and WC), the temperatures are stable within $<$5°C of the mean.

4.2. Episodic Variability: Stochasticity of Abrupt Temperature Excursions

4.2.1. High Temperature

As mentioned above, some of the HT records and most of the IT records exhibit abrupt, episodic, temperature excursions. Episodic perturbations observed in HT records consist primarily of abrupt temperature drops followed by a gradual recovery to the original exit temperature. Figure 6a shows four representative examples from the set of 52 episodic events observed in the HT records, with temperature drops (DT) ranging from 3 to ~160°C from the initial temperature T_0. We characterize the events by identifying the time required to reach the minimum temperature (t_1) and then the time required for the temperature to recover 95% of temperature drop DT (t_2). The HT episodic events have typical durations of a few hours (with a few lasting up to ~2–3 days) with t_2/t_1 typically $<$20 (70% of t_2/t_1 $<$10, Figures 6b and 6c). We do not observe any correlation between the magnitude of the temperature drop with neither the event duration nor t_2/t_1.

The HT records also display a few temperature increases, as shown in Figure 6d for the Montsegur site in the 2009–2010 deployment. These events are markedly different from the cooling events, and displaying temperature increases of up to 10°C spanning over 4–6 days. In contrast, the temperature drop is sudden and

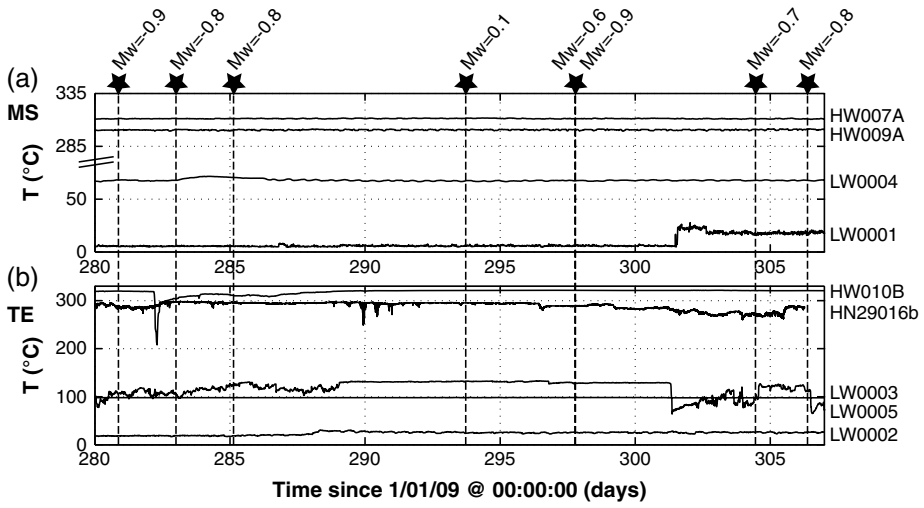

Figure 7. Examples of high- and low-temperature records installed in MS (a) and TE (b) over a 27 days time window. Names of probes are indicated at the right of the records. Earthquakes with magnitude >-1 and occurring below the field are shown by black stars and dashed lines, together with their magnitude. Note that there is no correlation between variations in the temperature of fluid outflow among records, nor with seismicity.

spans over ~1 day, with the temperature returning to that at the start of the event. Owing to the scarce number of such events, it is not possible to statistically characterize them.

4.2.2. Intermediate Temperature

In Figures 6e, 6f, and 6g, we show examples of 40 day-long IT records displaying both warming and cooling events. Exit-fluid temperatures in the IT records exhibit rapid increases and decreases of up to several tens of °C but with no subsequent recovery to pre-event levels. In Figure 6e, following a sharp drop of ~80°C (black line), there is a succession of warming events with excursions of several tens of degrees and of a shape that is similar to that observed in the HT records (Figure 6d). Figure 6f shows in contrast a warming event followed up by temperature variations spanning over ~20°C, where no clear baseline can be defined. Finally, Figure 6g, a third type of variability in IT records is characterized by recurrent temperature peaks above background seawater temperature (baseline).

4.2.3. Site and Inter-Site Variability and Link With Microseismicity

We illustrate the lack of intra- and inter-sites correlation in the episodic temperature perturbations by showing a ~25 day interval of records from the Montsegur (Figure 7a) and Tour Eiffel sites (Figure 7b). Although the records from each site were acquired from closely spaced sensors at different outflows, there is no relationship

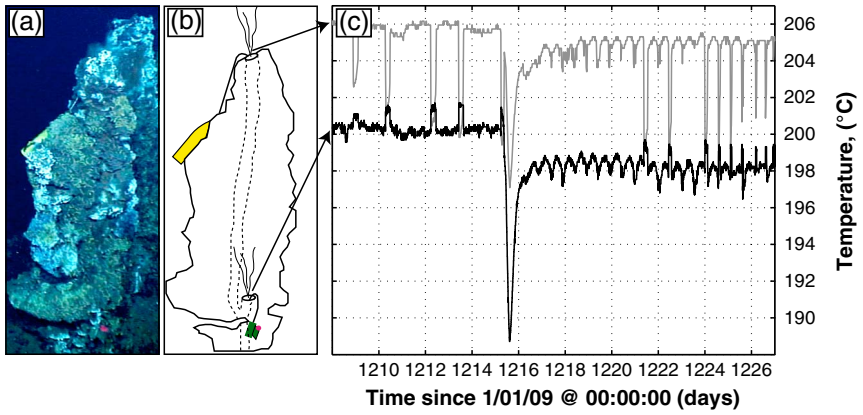

Figure 8. (a) ROV video frames of two probes (HW0009 at the top of the chimney and HN30009 at the base of the chimney) installed in two different vents from the same chimney structure and deployed in 2011 (MoMARSAT11) and recovered in 2012 (MoMARSAT12, right). (b) Sketch of (a) to indicate the measure points and placement of instruments. (c) Temperature records of probes HW0009 (gray, top of chimney) and HN30009 (black, bottom of chimney).

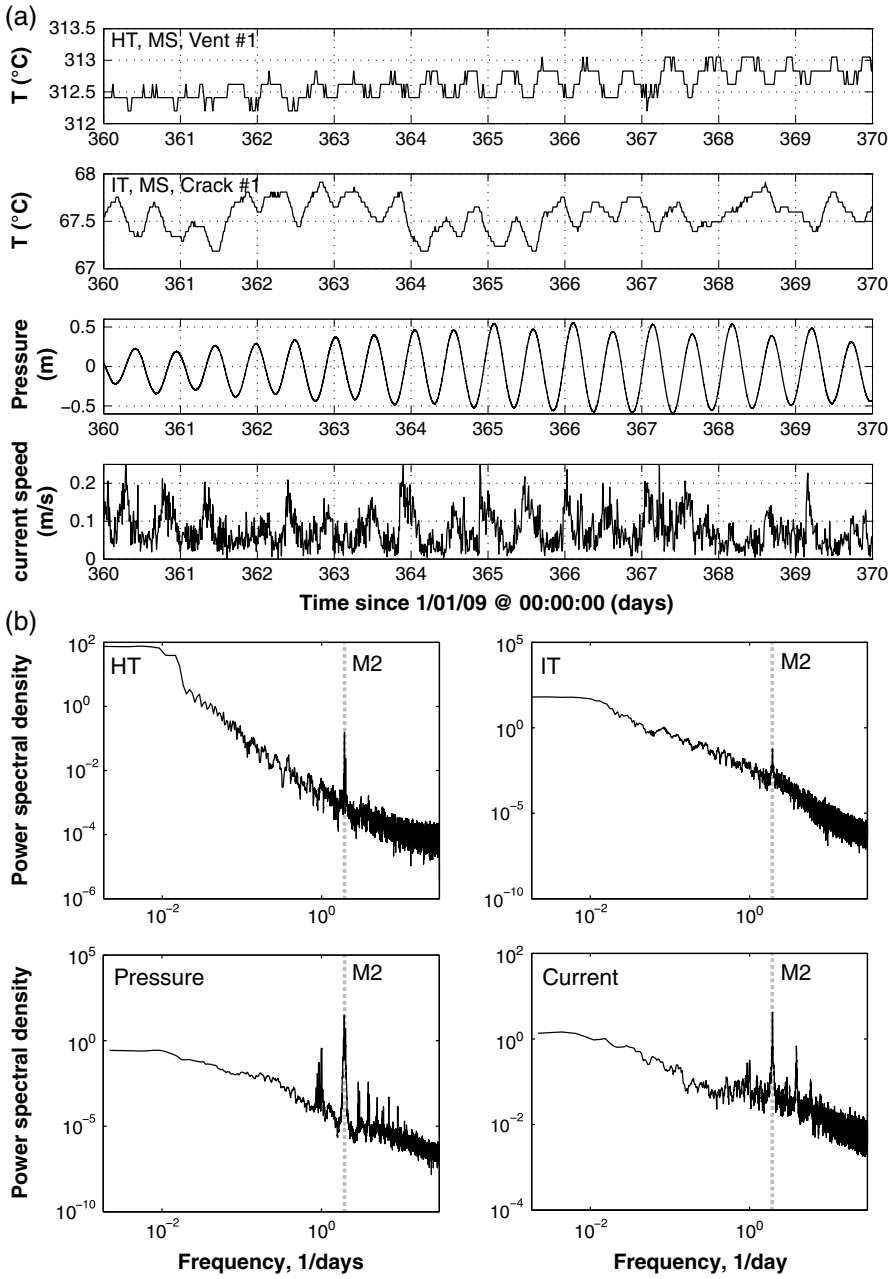

Figure 9. (a) Tidal signature illustrated over a 10 day time window on HT and IT records at Montsegur hydrothermal mound (top two plots), and the corresponding variations in bottom pressure and current speed (bottom two plots). (b) Corresponding power spectra for the pressure, current, HT, and IT records shown. Spectral analysis was made by using the multi-taper method described by *Thomson* [1982]. The frequency of the main semi-diurnal tidal harmonic M2 is shown as gray dashed line. Note that the M2 frequency peak is clearly visible in both temperature spectra but exhibits less power in the intermediate-temperature one.

between the observed variations in discharge temperature. We note that the numerous temperature drops in HT record HN29016b (TE, Figure 7b) are not correlated with any events in the other HT and IT records acquired nearby (horizontal distances of $<$10 m) at this site. The HT records at the MS site (Figure 7a) are very stable and lack any temperature excursions during this period of time that may be correlated with those observed at TE.

Figure 8 illustrates the only instance where we observed correlation of temperature events between two records, one at its summital vent, and the other at a vent a few meters below on the flank of the same chimney at Sintra (Figures 8a and 8b). These records show a periodic, tidal variability of ~0.5–1°C. Over-imposed, there are cooling and warming events that are anti-correlated, and with excursions of up to ~5°C and ~2°C

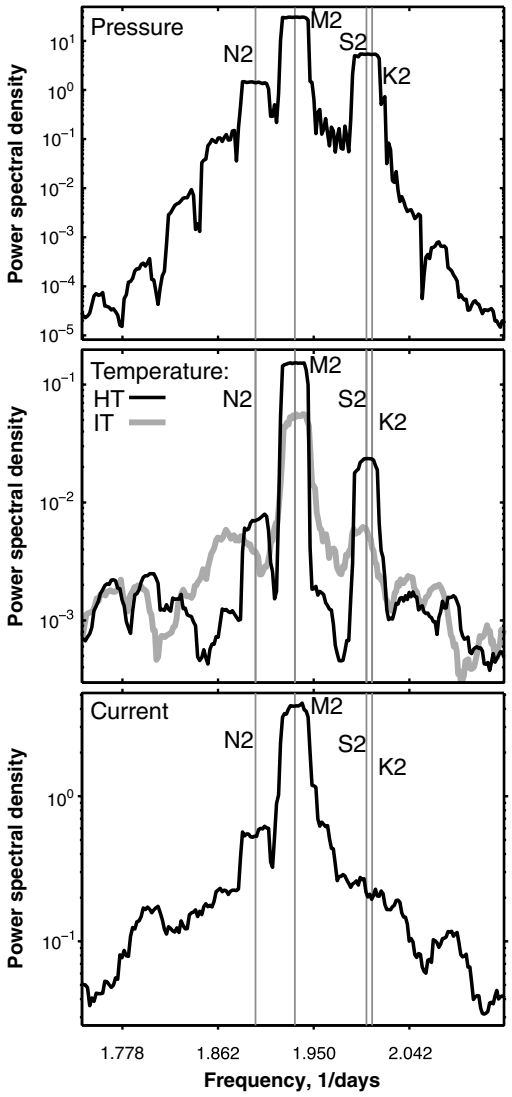

Figure 10. Detail of power spectral density (PSD) plots around the semi-diurnal harmonics peaks for pressure, current, and temperature (HT in solid line and IT in thick gray line). N2 (major lunar elliptic), M2 (principal lunar), S2 (principal solar), and K2 (luni-solar declination) are shown by gray solid lines. Note that S2 and K2 peaks are absent of the current power spectra and are very low amplitude or inexistent in the spectra from the intermediate-temperature record.

in amplitude, respectively (Figure 8c). A more pronounced cooling of up to 10°C is observed in both temperature records at day ~1215. This more pronounced cooling event likely represents a perturbation taking place below the two sensors and affecting both of them.

We also document an apparent lack of correlation between temperature events and microseismicity recorded by Ocean Bottom Seismometer (OBS) network deployed contemporaneously [*Crawford et al.*, 2013]. Figure 7 shows the origin time for the eight largest microearthquakes ($M_w > -1$) observed in the study area above the melt lens for this time window. None of the microearthquakes affected discharge temperatures at the measurement sites, even taking into account a delay response to the temperature records (4–5 days delay following a seismic event at the EPR [*Sohn et al.*, 1998]). Several HT records lack any temperature excursions and therefore demonstrate that the observed seismicity did not impact the outflow at these sites (Figure 7). Thus, we find that the episodic temperature variations in the HT and IT records are uncorrelated between measurement sites at field and inter-site length scales, and they are also uncorrelated with microearthquake activity underlying LSHF.

4.3. Periodic Variability at Tidal Frequencies

All of the temperature records exhibit periodic variability at tidal frequencies as shown in selected HT and IT time series data and spectral estimates (Figures 9 and 10). While the full range of tidal frequencies (fortnightly, diurnal, semi-diurnal, etc.) are found in the pressure and current records, the temperature records only exhibit variability at semi-diurnal frequencies (Figure 9b). We also note the lack of power in the inertial or 4 cpd bands in both current and temperature records. The detailed frequency response at semi-diurnal periods is shown in Figure 10, including the principal lunar semi-diurnal (M_2), the major lunar elliptic (N_2), the principal solar (S_2), and the luni-solar declination (K_2) frequencies. The four main semi-diurnal tidal frequencies are observed in the HT records (M_2, S_2, N_2, and K_2) and are also visible in the IT records although with an overall lower power (Figure 10). In contrast, both S_2 and K_2 are absent from LT and current records. The amplitude of temperature variations at tidal frequencies is <0.5°C for the HT records (Figure 9a) and somewhat larger for the LT and IT records. We note that similar semi-diurnal temperature oscillations have been previously reported for IT and LT records from other hydrothermal fields (MEF at JdFR [*Tivey et al.*, 2002]; 9°50′N at EPR [*Scheirer et al.*, 2006]; TAG at MAR [*Sohn*, 2007a, 2007b]), and for HT records from an additional site (MEF at JdFR, [*Larson et al.*, 2007, 2009]).

We evaluated the relationship between tidal processes (pressure and current variations) and the temperature records by conducting cross-spectral analyses using the multi-taper method [*Thomson*, 1982]. Coherent variability between tidal processes (pressure and current) and the exit-fluid temperature records is restricted to the semi-diurnal band. For tidal pressure, the highest levels of coherency are observed with HT records at

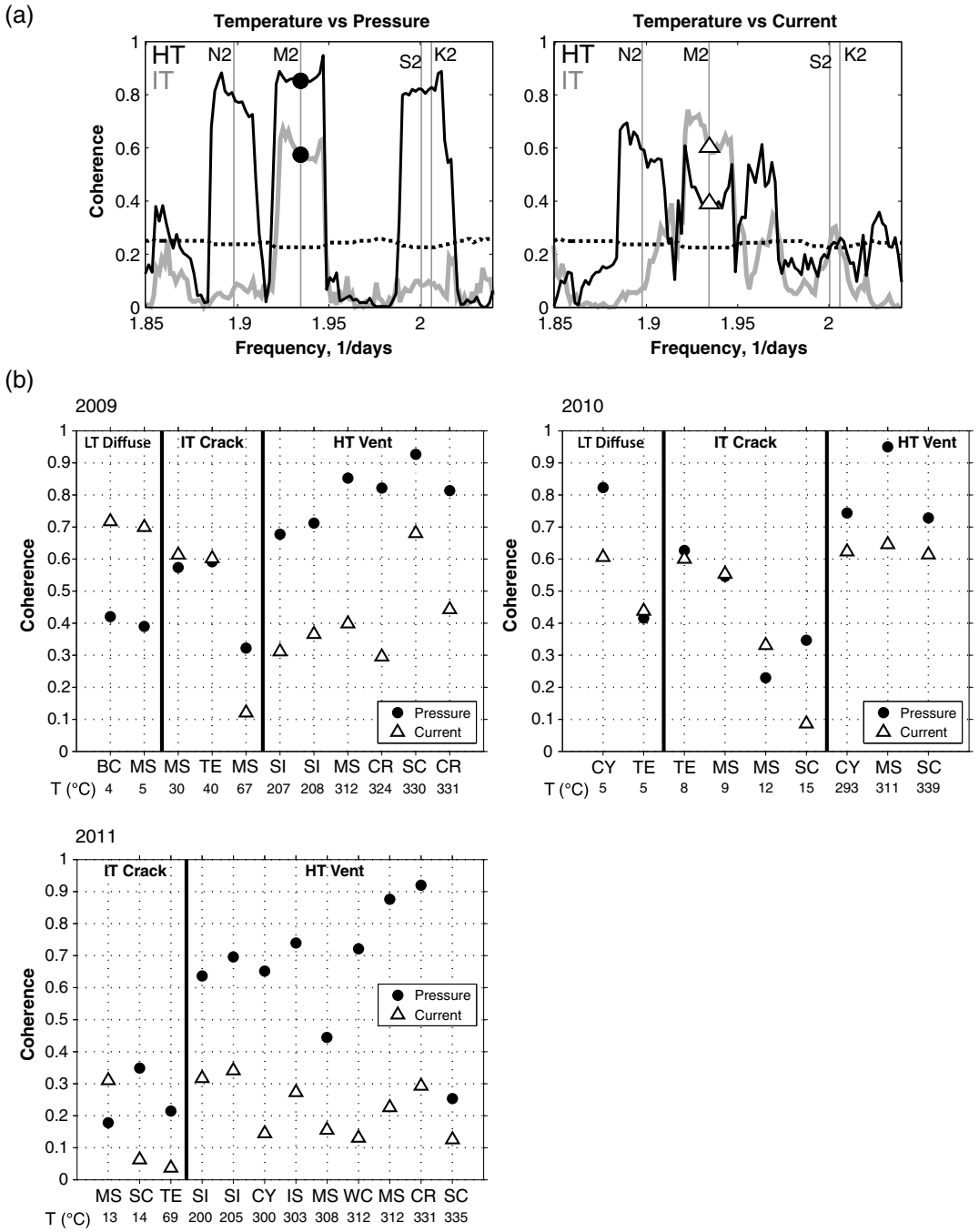

Figure 11. (a) Examples of coherence calculation between both high- (black) and intermediate-temperature (gray) and pressure (left) and current (right). Circles indicate coherence with pressure at the M2 frequency, while triangles indicate the coherence with current at the same frequency. Zero significant level (zsl), calculated for 90% confidence, is shown by a black dashed line on both subplots. Semi-diurnal harmonics N2, M2, S2, and K2 are shown by thin vertical lines. (b) Coherence for selected records (2009–2010, 2010–2011, and 2011–2012) with pressure (black circles) and current (white triangles). Temperature records are arranged by increasing average temperature (indicated below) with names of sites where probes were, and black lines show separation between high-, intermediate-, and low-temperature records. Records used in coherence calculations are indicated in Table 2 with an asterisk behind probe names.

the M_2 frequency, although coherency with HT records is also observed at the N_2, S_2, and K_2 tidal frequencies (Figure 11a, left). IT records show significantly lower coherency at the M_2 frequency than HT records and lack coherency at the S_2 and K_2 tidal frequencies (Figure 11a, left). For tidal currents, the coherence for the IT

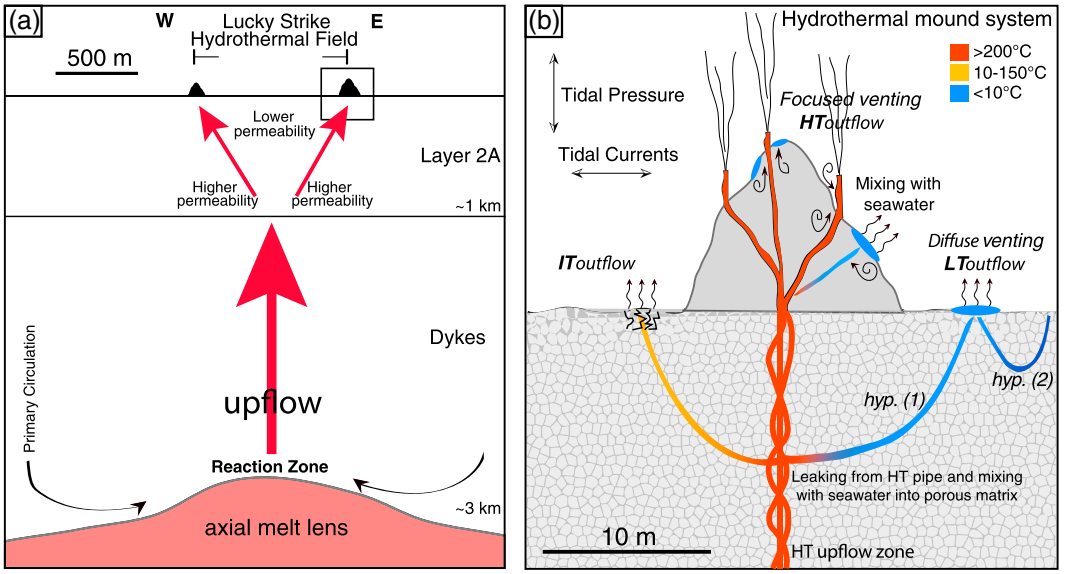

Figure 12. (a) Conceptual model of the Lucky Strike hydrothermal plumbing system structure at depth, with the upwelling of a single plume above the AMC that is focused along high-porosity areas associated with the main faults bounding axial graben. Figure 12b is a zoom at the hydrothermal edifice (black box on Figure 12a), showing our interpretation of the origin of the LT, IT, and HT regimes. With HT outflow directly fed by the high-temperature upflow zone (here represented as an anastomosing, interconnected series of conduits), IT outflow fed from leakage from the HT pipe and mixed with cold water into the porous matrix (i.e., hypothesis (1)) and LT outflow fed from either hypothesis (1) or conductively heated bottom water drawn into the seafloor as part of the secondary circulation system (i.e., hypothesis (2)).

records is similar to that with the pressure and lack coherency at the N_2 constituent (Figure 11a, right). HT records exhibit lower coherency with currents than with pressure but display coherency peaks at the N_2, S_2, and K_2 constituents (Figure 11a, right).

Figure 11b reports the set of coherency estimates at the M_2 frequency between discharge temperature and both tidal pressure and current for different sites throughout the LSHF for each of the three annual deployment intervals (coherency estimates for 2010–2011 and 2011–2012 limited to ~110 days of data owing to logging issues, as described in section 3.4). These data demonstrate that semi-diurnal variability in the HT records is in all cases significantly more coherent with tidal pressure than tidal current.

By contrast, the results for the IT and LT records are less systematic. Coherency levels for IT records are consistently lower than those observed for HT records for both pressure and currents, with some records showing higher coherency with pressure, others with currents, and the remaining displaying indistinguishable coherency.

We only have coherency estimates for four LT temperature records (installed over algal mats, Figures 2e and 2f): two from the 2009–2010 deployments at MS and BC, and two from the 2010–2011 deployments at TE and CY. The LT records from MS and BC in 2009 are clearly more coherent with tidal currents compared to pressure, while the LT records from TE and CY in 2010 are equally or more coherent with pressure. We consider the 2009 estimates to be more robust because they are derived from a full year of data (compared to ~110 days of data for 2010), but it is clear that we do not have enough records (4) to establish systematic LT behavior at tidal periods.

5. Discussion

Our results provide new information regarding the impact of tidal processes on exit-fluid temperatures at deep-sea vent fields, and they also provide new constraints on the nature of episodic excursions observed in the temperature records. We discuss these topics and the overall implications for hydrothermal circulation and discharge at the LSHF, below.

5.1. Temperature Records and the Subseafloor Circulation System at Lucky Strike

Hydrothermal circulation in young oceanic crust at MORs is typically conceptualized as consisting of a primary system, which extracts heat from a deep-seated, likely magmatic heat source (i.e., AMC) (Figure 12a),

and a secondary circulation system driven by conductive heat transfer across impermeable (e.g., mineralized) conduit walls from hot fluid in the primary system to cold pore fluids in the shallow subsurface [e.g., *Lister*, 1980; *Cann and Strens*, 1989; *Lowell et al*., 1995, 2007; *Van Dover*, 2000; 2007; *Germanovich et al*., 2011]. A model of hydrothermal circulation and discharge at the seafloor for the Lucky Strike hydrothermal field, based on the temperature records analyzed here and prior work on photomosaics, is illustrated on Figure 12. Analysis of seafloor mosaics has shown that hydrothermal outflow is clustered into two major zones, east and west of LSHF (Figure 12a) [*Barreyre et al*., 2012]. Based on the association of individual outflow zones to fault scarps, this clustering of sites is consistent with the axial graben faults acting as permeable pathways for ascending fluids [*Barreyre et al*., 2012]. Primary hydrothermal fluids in a mature hydrothermal system such as Lucky Strike are believed to rise essentially unmixed and nearly adiabatically from a water-rock reaction zone above the roof of the magmatic heat source to the shallow crust [*Bischoff and Rosenbauer*, 1989; *Wilcock*, 1998]. Some of these fluids may pass through the shallow, permeable crust along a zone of anastomosing conduits or a single one that is isolated from the host rock, discharging at the seafloor at high temperatures with essentially no mixing. The rest of the fluids may leak into fractures and porosity within the rock hosting the plumbing system of the hydrothermal field. This geometry may promote mixing with cold pore fluids (seawater) prior to discharge. Based on the overall stability of some of the HT records acquired at the LSHF (Figure 4c, top, and Table 2), we attribute these to the unmixed, primary fluids. Mixing in the upper crust is likely to lead not only to lower outflow temperatures but also to a more unstable and variable flow pattern, consistent with the characteristics of the IT records. Fluid temperatures in the IT records may thus be controlled by the mixing proportions of primary hydrothermal fluid and cold fluid (either pore fluids or seawater). The proportion of hydrothermal end-member fluid may range from ~30% to $<$5% (assuming temperatures of ~350°C and ~4°C for hydrothermal end-member fluid and seawater, respectively), consistent with prior estimates of $<$10% of hydrothermal end-members in the area [*Cooper et al*., 2000].

The LT records, acquired over bacterial mats, display tidal modulated temperature variations associated with the interaction between currents and the seepage of warm fluids through the seafloor, thus strongly controlling the environmental condition where bacterial mats develop [e.g., *Crépeau et al*., 2011]. These temperature variations are associated with the evolution of the thermal boundary layer formed by these warmer fluids, which can have two different origins. The warm fluids could represent mixing of primary, high-temperature fluids with cold pore fluids due to near-surface leaks in primary conduits (hypothesis (1) in Figure 12b). Alternatively, they could represent conductively heated bottom water drawn into the seafloor as part of the secondary circulation system (hypothesis (2) in Figure 12b) [*Lowell et al*., 2007, 2013; *Cooper et al*., 2000].

5.2. Tidal Modulation of Exit-Fluid Temperature

All of the temperature records that we acquired at the LSHF exhibit variability at tidal frequencies and lunar semi-diurnal periods, in particular. This is consistent with previous results from other deep-sea vent fields [e.g., *Tivey et al*., 2002; *Scheirer et al*., 2006; *Sohn*, 2007a; *Larson et al*., 2007, 2009]. In addition, and in contrast with these previous studies, we contemporaneously measured bottom pressure, bottom currents, and discharge temperatures, allowing us to distinguish between the competing effects of tidal pressure and current as forcing functions for the temperature records.

Our cross-spectral analyses demonstrate that there are systematic relationships between tidal forcing and exit-fluid temperature that vary according to the hydrogeology of the measurement site (Figure 11). The most striking result is the systematic relationship between tidal pressure and exit-fluid temperature in the HT records. All of the HT records are significantly more coherent with tidal pressure than tidal currents at semi-diurnal frequencies, providing strong evidence that the poroelastic effects of tidal loading modulate discharge temperatures, and therefore vertical flow velocities [*Jupp and Schultz*, 2004; *Crone and Wilcock*, 2005]. Our cross-spectral analyses represent the first time that this relationship has been unequivocally established for a deep-sea vent field.

In contrast to the HT records, the IT and LT records exhibit more complex behaviors at tidal periods, with overall lower coherencies between discharge temperature and tidal forcing and no systematic behavior relative to tidal pressure vs. current. The IT records exhibit a transitional type behavior, with some correlating more strongly with tidal pressure, others correlating more strongly with tidal current, and the remaining displaying a control by both tidal currents and pressures. Although the data available from the LT sites is limited,

the cross-spectral analyses suggest that these records are most strongly correlated with tidal currents. More data are clearly needed to test this assertion, but the LT records clearly do not respond to tidal pressure in the same systematic way as the HT records.

We interpret the cross-spectral results in terms of the hydrogeology of the measurement sites and the presence of two end-member fluids. If tidal pressure affects vertical flow velocities and thus exit-fluid temperatures in the rising limb of the primary circulation system as hypothesized and modeled previously [*Jupp and Schultz*, 2004; *Crone and Wilcock*, 2005], then the hot hydrothermal end-member (that does not mix during ascent to the seafloor) will exhibit discharge temperatures that correlate most strongly with tidal pressure (i.e., the HT records). By contrast, the temperature of ambient seawater (the cold end-member, and therefore of the boundary layer) in the deep sea is primarily controlled by currents. Thus, the LT and IT records can be sensitive to both tidal pressure and current, as they measure fluids discharging with variable mass fractions of the ambient seawater end-member, or modify the efficiency of conductive heating.

Based on limited existing studies, the observed patterns of coherence between temperature and both pressure and current may to some degree be specific to the LSHF because tidal loading and bottom currents can have very different signatures in other oceanographic settings. For example, on the Cleft segment of the Juan de Fuca Ridge, *Tivey et al*. [2002] report that diffuse outflow is modulated by bottom currents, but the period of variability corresponded to inertial, rather than tidal, currents. This suggests that the local hydrography controlling tides and associated currents will play a major role on the temporal variability of diffuse outflow. Furthermore, no tidal signals were observed in the high-temperature records from this same Cleft site [*Tivey et al*., 2002], which could reflect differences in the amplitude of tidal forcing, in subsurface hydrogeology, crustal permeability, or any combination of these.

5.3. Origin of Episodic Variability

The sudden, episodic changes in temperature observed both in HT and IT records are likely related to very shallow processes that modify the overall mass fraction of the cold water end-member at a given measurement site. The primary argument for shallow perturbation processes is the lack of correlation between episodic changes observed both across the field and between closely spaced probes at different vents within a given site (Figure 7). Second, there is no correlation with deep-seated processes such as microearthquakes occurring near the inferred reaction zone, above the AMC roof [*Crawford et al*., 2013]. Owing to their small magnitude (typically $Mw<1$), the microearthquake rupture length is likely to be very small (<10 m [*Tomic et al*., 2009]) and therefore insufficient to modify circulation at the scale of the LSHF. We would expect a field-wide perturbation to occur only if larger magnitude events, or swarms, occurred within the circulation system. The only temperature records showing event correlations were acquired in the same chimney (Sintra, Figure 8). The anti-correlated temperature excursions are likely linked to perturbation of flow within the chimney itself and therefore recorded by both sensors. We therefore conclude that these perturbations are the result of highly localized processes near the measurement site, at length scales smaller than individual hydrothermal sites (e.g., at the scale of individual outflow conduits).

At the high-temperature sites, the episodic perturbations are transient, such that the discharge temperature eventually returns to pre-drop levels (Figure 6a) over a period of up to a few days (<10 days for most of the events identified). The episodic changes at the high-temperature sites are almost exclusively negative (i.e., temperatures drop) because the stable temperatures represent essentially unmixed primary fluids, such that an increase in the cold-water end-member causes temperatures to drop. These changes are likely due to mineralization and/or small-scale changes in chimney morphology (e.g., partial collapse, small-scale cracking), suddenly modifying the hydrothermal outflow. For example, if a chimney partially collapses the fluid flow may be temporarily perturbed resulting in a mixing with seawater and a related temperature drop. Subsequent recovery of temperature could be achieved by mineralization and rebuilding of the perturbed area or broken chimneys, restoring the unmixed high-temperature fluid flow regime.

Episodic temperature perturbations in the IT records are different in that they can be either positive or negative, are much more frequent than in HT records, and the temperature does not recover to pre-perturbation levels. The episodic perturbations are essentially step functions that change the mean discharge temperature until the next episodic event and that are superimposed on higher-frequency variability at time scales of a few minutes to few hours.

If the discharge temperature in IT records is controlled by the mixing of hot, primary, hydrothermal fluids with colder seawater, as we propose, then these sudden temperature changes most likely represent a change in the mixing proportions of the two end-member fluids. As with the HT perturbations, the IT perturbations are not correlated among probes within a single site or across sites, suggesting again that the perturbations in hydrothermal outflow are highly localized and in the shallowest part of the system. The higher-frequency variability can therefore correspond to turbulent mixing, either arising from turbulent flow and therefore inhomogeneous mixing in the shallowest subseafloor, or to turbulence at the seafloor and within the boundary layer, resulting in seawater mixing with hydrothermal fluids.

The lack of episodic variability in the LT records can be explained largely by the fact that there is always a high proportion of cold bottom water in these measurements and that they are not deployed in mineralized cracks or chimneys that can change morphology over short periods of time. The lack of sudden perturbations may also support interpretation of the LT records as representing conductively heated fluids in the secondary circulation system, since conductive heating will not be sensitive to small details in the permeability structure.

5.4. Long-Term Variation of Discharge Temperatures

The ensemble set of HT temperature records over a 3 year period acquired from the Lucky Strike hydrothermal field suggest that the average outflow temperature associated with primary hydrothermal circulation is overall stable. Measured trends from individual records display variability even at a single site but are typically $<$3°C/yr (Table 2). These gradients are consistent with those inferred from the composite records for each of the deployments (Figure 5), which display gradients of 0.1 and 0.7°C for the 2009–2010 and 2011–2012 deployments. These values can be considered as reflecting a stable temperature, as the standard deviation of the composite records is large relative to the gradients (~1.5°C, Figure 5). This stability is also supported by the discrete temperature measurements at individual vents during the last ~20 years, reported in Table 3. Of all the vents monitoring since the mid-1990s, all are stable except for Statue of Liberty, which became inactive sometime between 1996 and 2009 (Table 3) [*Barreyre et al.*, 2012]. From both the temperature records and the historical temperature measurements, we conclude that the temperature of fluid discharge associated with the primary hydrothermal circulation at Lucky Strike has been stable at time scales from 3 to 20 years.

Optical photomosaics throughout the Lucky Strike hydrothermal field [*Escartín et al.*, 2008; *Garcia et al.*, 2011; *Barreyre et al.*, 2012] document a slight decrease of diffuse hydrothermal outflow at time scales of 1–10 years. This decrease is indicated by a decline in the surface area of diffuse discharge [*Barreyre et al.*, 2012] at numerous sites throughout LSHF. The overall constant outflow temperature (this work) and the apparent decrease in the diffuse hydrothermal outflow [*Barreyre et al.*, 2012] can be explained by an overall mild decrease in the mass flux and associated heat flux, (e.g., associated with a focusing of flow), which does not impact the temperature of the end-member hydrothermal fluid. Other observations supporting this decrease are the extinction of certain vents over time (e.g., Statue of Liberty [*Langmuir et al.*, 1997; *Barreyre et al.*, 2012]) and visual reports of overall decrease in activity, particularly at the diffuse outflow sites (2009 through 2012 yearly cruises to LHSF). Lacking systematic and extensive flowmeter measurements over time, we are unable to independently verify these apparent mass and heat fluxes decrease at the ~20 to 3 year time scales investigated.

6. Conclusions

1. We identify three distinct hydrothermal outflow regimes: (1) HT ($>$~200°C) sites representing essentially unmixed, primary, hydrothermal fluids, (2) IT (10–100°C) sites representing variable mixing proportions of primary fluids with cold seawater within permeable shallow crust, and (c) LT ($<$10°C) sites representing the thermal boundary layer at the seafloor formed by diffuse discharge of warm fluids interacting with cold bottom water.
2. Cross-spectral analyses reveal that HT discharge is modulated by tidal pressure rather than current, while the low-temperature fluids are influenced by tidal currents instead. IT discharge is variably modulated by both pressure and current, consistent with higher mass fractions of the cold seawater end-member.
3. Episodic perturbations observed in HT and IT records are generated by shallow, highly localized processes at the measurement sites that affect the mixing proportions of the end-member fluids.
4. The average temperature of the HT records, which are believed to represent end-member fluids, vary (both positive and negative) over annual time-scales, but the average temperature of the LSHF, as a whole, appears to have been stable over the 3 year observation period.

Acknowledgments

We thank the captain, officers, and crew on board N/O Pourquoi Pas? who made the series of Lucky Strike cruises possible. We thank the ROV Victor Team for supporting our deep submergence field campaign. We also thank Timothy Crone, Michael Hutnak, and an anonymous reviewer for detailed and insightful reviews. This project was funded by CNRS/IFREMER through the 2009, 2010, 2011, and 2012 cruises within the MoMAR program (France) and by ANR (France) Mothseim Project NT05-3 42213, led by J. Escartín. T. Barreyre was supported by University Paris Diderot (Paris 7—France) and Institut de Physique du Globe de Paris (IPGP, France), IPGP contribution 3443.

References

Ballu, V., et al. (2009), A seafloor experiment to monitor vertical deformation at the Lucky Strike volcano, Mid-Altantic Ridge, *J. Geod.*, doi:10.1007/s00190-008-0248-3.

Barreyre, T., J. Escartín, R. Garcia, M. Cannat, E. Mittelstaedt, and R. Prados (2012), Structure, temporal evolution, and heat flux estimates from the Lucky Strike deep-sea hydrothermal field derived from seafloor image mosaics, *Geochem. Geophys. Geosyst.*, *13*, Q04007, doi:10.1029/2011GC003990.

Bischoff, J. L., and R. J. Rosenbauer (1989), Salinity variations in submarine hydrothermal systems by layered double-diffusive convection, *J. Geol.*, *97*, 613–623.

Cann, J., and M. R. Strens (1989), Modeling periodic megaplume emission by black smoker systems, *J. Geophys. Res.*, *94*, 12,227–12,237.

Charlou, J. L., J. P. Donval, E. Douville, P. Jean-Baptiste, J. Radford-Knoery, Y. Fouquet, A. Dapoigny, and M. Stievenard (2000), Compared geochemical signatures and the evolution of Menez Gwen (37°50′N) and Lucky Strike (37°17′N) hydrothermal fluids, south of the Azores Triple Junction on the Mid-Atlantic Ridge, *Chem. Geol.*, *171*(1–2), 49–75.

Combier, V. (2007), *Mid-Ocean Ridge Processes: Insights From 3D Reflection Seismics at the 9°N OSC on the East Pacific Rise, and the Lucky Strike Volcano on the Mid-Atlantic Ridge*, 261 pp., Inst. de Phys. du Globe, Paris, France.

Cooper, M. J., H. Elderfield, and A. Schultz (2000), Diffuse hydrothermal fluids from Lucky Strike hydrothermal vent field: Evidence for a shallow conductively heated system, *J. Geophys. Res.*, *105*, 19,369–19,375.

Corliss, J. B., et al. (1979), Submarine Thermal Springs on the Galapagos Rift, *Science*, *203*(4385), 1073–1083.

Crawford, W. C., A. Rai, S. C. Singh, M. Cannat, J. Escartin, H. Wang, R. Daniel, and V. Combier (2013), Hydrothermal seismicity beneath the summit of Lucky Strike volcano, Mid- Atlantic Ridge, *Earth Planet. Sci. Lett.*, *373*, 118–128, doi:10.1016/j.epsl.2013.04.028i.

Crépeau, V., M. A. Cambon Bonavita, F. Lesongeur, H. Randrianalivelo, P. M. Sarradin, J. Sarrazin, and A. Godfroy (2011), Diversity and function in microbial mats from the Lucky Strike hydrothermal vent field, *FEMS Microbiol. Ecol.*, *76*, 524–540.

Crone, T. J., and S. D. Wilcock (2005), Modeling the effects of tidal loading on mid-ocean ridge hydrothermal systems, *Geochem. Geophys. Geosyst.*, *6*, Q07001, doi:10.1029/2004GC000905.

Davis, E., and K. Becker (1999), Tidal pumping of fluids within and from the oceanic crust: New observations and opportunities for sampling the crustal hydrosphere, *Earth Planet. Sci. Lett.*, *172*, 141–149.

Donval, J. P., J. L. Charlou, E. Douville, J. Knoery, Y. Fouquet, E. Ponzeverra, P. Jean-Baptiste, M. Stievenard, and C. R. German (1997), The Flores Scientific Party, High H_2 and CH_4 content in hydrothermal fluids from Rainbow site newly sampled at 36°14′N on the Amar segment, Mid-Atlantic Ridge (diving Flores cruise, July 1997), *Eos Trans*, *78*, 832, (abstr).

Escartín, J., R. García, O. Delaunoy, J. Ferrer, N. Gracias, A. Elibol, X. Cufi, D. J. Fornari, S. E. Humphris, and J. Renard (2008), Globally-aligned photo mosaic of the Lucky Strike hydrothermal Vent Field (Mid-Atlantic Ridge, 37°18.5′N): Release of geo-referenced data, mosaic construction and viewing software, *Geochem. Geophys. Geosyst.*, *9*, Q12009, doi:10.1029/2008GC002204.

Fofonoff, N. P., and R. C. Millard Jr. (1983), Algorithms for computation of fundamental properties of seawater, Unesco Technical Papers in Marine Science, No. 44, 53 pp.

Fontaine, F. J., M. Cannat, and J. Escartin (2008), Hydrothermal circulation at slow-spreading mid-ocean ridges: The role of along-axis variations in axial lithospheric thickness, *Geology*, *36*, 759–762, doi:10.1130/G24885A.1.

Fornari, D. J., F. Voegeli, and M. Olsson (1996), Improved low-cost, time-lapse temperature loggers for deep ocean and sea floor observatory monitoring, *RIDGE Events*, *7*, 13–16.

Fornari, D., C. L. Van Dover, T. Shank, R. Lutz, and M. Olsson (1994), A versatile, low-cost temperature sensing device for time-series measurements at deep sea hydrothermal vents, *BRIDGE Newslett.*, *6*, 37–40.

Fornari, D. J., T. Shank, K. L. Von Damm, T. K. P. Gregg, M. Lilley, G. Levai, A. Bray, R. M. Haymon, M. R. Perfit, and R. Lutz (1998), Time-series temperature measurements at high-temperature hydrothermal vents, East Pacific Rise 9°49′-51′N: Evidence for monitoring a crustal cracking event, *Earth Planet. Sci. Lett.*, *160*, 419–431.

Fouquet, Y., H. Ondreas, J. L. Charlou, J. P. Donval, J. Radford-Knoery, I. Costa, N. Lourenço, and M. K. Tivey (1995), Atlantic lava lakes and hot vents, *Nature*, *377*, 201.

Garcia, R., R. Campos, and J. Escartín (2011), High-resolution 3D reconstruction of the seafloor for environmental monitoring and modelling, paper presented at IEEE/RSJ International Conference on Intelligent Robots and Systems, Workshop on Robotics for Environmental Monitoring, Inst. of Electr. and Electron. Eng., San Francisco, Calif.

Germanovich, L. N., R. P. Lowell, and D. K. Astakhov (2001), Temperature-dependent permeability and bifurcations, in hydrothermal flow, *J. Geophys. Res.*, *106*, 473–495.

Germanovich, L. N., R. P. Lowell, and D. K. Astakhov (2000), Stress-dependent permeability and the formation of seafloor event plumes, *J. Geophys. Res.*, *105*, 8341–8354.

Germanovich, L. N., R. P. Lowell, and P. Ramondenc (2011), Magmatic origin of hydrothermal response to earthquake swarms: Constraints from heat flow and geochemical data at 9°50′N, East Pacific Rise, *J. Geophys. Res.*, *116*, B05103, doi:10.1029/2009JB006588. [Available at http://tos.org/oceanography/archive/25-1_lowell.html#sthash.ShzNb2U3.dpuf.]

Gribbin, J. L., W. Zhu, and M. K. Tivey (2012), Anisotropy in seafloor flange, slab, and crust samples from measurements of permeability and porosity, Implications for fluid flow and deposit evolution, *Geochem. Geophys. Geosyst.*, *13*, Q03018, doi:10.1029/2011GC003840.

Han, L., R. P. Lowell, and K. C. Lewis (2013), The dynamics of two-phase hydrothermal systems at a seafloor pressure of 25 MPa, *J. Geophys. Res. Solid Earth*, *118*, 1–13, doi:10.1002/jgrb.50158.

Humphris, S. E., D. J. Fornari, D. S. Scheirer, C. R. German, and L. M. Parson (2002), Geotectonic setting of hydrothermal activity on the summit of Lucky Strike seamount (37° 17′N, Mid-Atlantic Ridge), *Geochem. Geophys. Geosyst.*, *3*(8), 1049, doi:10.1029/2001GC000284.

Johnson, H. P., M. Hutnak, R. P. Dziak, C. G. Fox, I. Urcuyo, J. P. Cowen, J. L. Nabelek, and C. Fisher (2000), Earthquake-induced changes in a hydrothermal system on the Juan de Fuca mid-ocean ridge, *Nature*, *407*, 174–177.

Jupp, T. E., and A. Schultz (2004), A poroelastic model for the tidal modulation of seafloor hydrothermal systems, *J. Geophys. Res.*, *109*, B03105, doi:10.1029/2003JB002583.

Kinoshita, M., R. P. Von Herzen, O. Matsubayashi, and K. Fujioka (1998), Erratum to 'Tidally-driven effluent detected by long-term temperature monitoring at the TAG hydrothermal mound, Mid-Atlantic Ridge [Phys. Earth Planet. Int. 108_1998/143–154], *Phys. Earth Planet. Inter.*, *109*, 201–212.

Langmuir, C., et al. (1997), Hydrothermal vents near a mantle hot spot: The Lucky Strike vent field at 37°N on the Mid-Atlantic Ridge, *Earth Planet. Sci. Lett.*, *148*, 69–91.

Larson, B. I., E. J. Olson, and M. D. Lilley (2007), In situ measurement of dissolved chloride in high temperature hydrothermal fluids, *Geochim. Cosmochim. Acta*, *71*, 2510–2523, doi:10.1016/j.gca.2007.02.013.

Larson, B. I., M. D. Lilley, and E. J. Olson (2009), Parameters of subsurface brines and hydrothermal processes 12–15 months after the 1999 magmatic event at the Main Endeavor Field as inferred from in situ time series measurements of chloride and temperature, *J. Geophys. Res.*, *114*, B01207, doi:10.1029/2008JB005627.

Lilley, M. D., D. A. Butterfield, J. E. Lupton, and E. J. Olson (2003), Magmatic events can produce rapid changes in vent chemistry, *Nature*, *422*, 878–881.

Lister, C. R. B. (1980), Heat flow and hydrothermal circulation, *Annu. Rev. Earth Planet. Sci.*, *8*, 95–117.

Lowell, R. P., and D. K. Burnell (1991), Mathematical modelling of conductive heat transfer from a freezing, convective magma chamber to a single-pass hydrothermal system: Implications for seafloor black smokers, *Earth Planet. Sci. Lett.*, *104*, 59–69.

Lowell, R. P., and L. N. Germanovich (1994), On the temporal evolution of high-temperature hydrothermal systems at ocean ridge crests, *J. Geophys. Res.*, *99*, 565–575.

Lowell, R. P., P. A. Rona, and R. P. Von Herzen (1995), Seafloor hydrothermal systems, *J. Geophys. Res.*, *100*, 327–352.

Lowell, R. P., S. Gosnell, and Y. Yang (2007), Numerical simulations of single-pass hydrothermal convection at mid-ocean ridges: Effects of the extrusive layer and temperature-dependent permeability, *Geochem. Geophys. Geosyst.*, *8*, Q10011, doi:10.1029/2007GC001653.

Lowell, R. P., A. Farough, J. Hoover, and K. Cummings (2013), Characteristics of magma-driven hydrothermal systems at oceanic spreading centers, *Geochem. Geophys. Geosyst.*, *14*, 1756–1770, doi:10.1002/ggge.20109.

Mittelstaedt, E., J. Escartín, N. Gracias, J.-A. L. Olive, T. Barreyre, A. Davaille, M. Cannat, and R. Garcia (2012), Quantifying diffuse and discrete venting at the Tour Eiffel vent site, Lucky Strike hydrothermal field, *Geochem. Geophys. Geosyst.*, *13*, Q04008, doi:10.1029/2011GC003991.

Ondréas, H., M. Cannat, Y. Fouquet, A. Normand, P.-M. Sarradin, and J. Sarrazin (2009), Recent volcanic events and the distribution of hydrothermal venting at the Lucky Strike hydrothermal field, Mid-Atlantic Ridge, *Geochem. Geophys. Geosyst.*, *10*, Q02006, doi:10.1029/2008GC002171.

Pester, N. J., E. P. Reeves, M. E. Rough, K. Ding, J. S. Seewald, and W. E. Seyfried (2012), Subseafloor phase equilibria in high-temperature hydrothermal fluids of the Lucky Strike Seamount (Mid- Atlantic Ridge, 37°17′N), *Geochim. Cosmochim. Acta*, *90*, 303–322, doi:10.1016/j.gca.2012.05.018.

Ramondenc, P., L. N. Germanovich, K. L. Von Damm, and R. P. Lowell (2006), The first measurements of hydrothermal heat output at 9°50′N, East Pacific Rise, *Earth Planet. Sci. Lett.*, *245*, 487–497.

Scheirer, D. S., T. M. Shank, and D. J. Fornari (2006), Temperature variations at diffuse and focused flow hydrothermal vent sites along the northern East Pacific Rise, *Geochem. Geophys. Geosyst.*, *7*, Q03002, doi:10.1029/2005GC001094.

Singh, S. C., W. C. Crawford, H. Carton, T. Seher, V. Combier, M. Cannat, J. P. Canales, D. Dusunur, J. Escartín, and J. M. Miranda (2006), Discovery of a magma chamber and faults beneath a Mid-Atlantic Ridge hydrothermal field, *Nature*, *442*, 1029–1032, doi:10.1038/nature05105.

Sleep, N. H. (1991), Hydrothermal circulation, anhydrite precipitations, and thermal structure of ridge axes, *J. Geophys. Res.*, *96*, 2375–2387.

Sohn, R. A. (2007a), Stochastic analysis of exit fluid temperature recrods from the active TAG hydrothermal mound (Mid-Atlantic Ridge, 26°N): 1. Modes of variability and implications for subsurface flow, *J. Geophys. Res.*, *112*, B07101, doi:10.1029/2006JB004435.

Sohn, R. A. (2007b), Stochastic analysis of exit fluid temperature records from the active TAG hydrothermal mound (Mid-Atlantic Ridge, 26°N): 2. Hidden Markov models of flow episodes, *J. Geophys. Res.*, *112*, B09102, doi:10.1029/2007JB004961.

Sohn, R. A., D. J. Fornari, K. L. Von Damm, J. A. Hildebrand, and S. C. Webb (1998), Seismic and hydrothermal evidence for a cracking event on the East Pacific Rise crest at 9°50′N, *Nature*, *396*, 159–161.

Thomson, D. J. (1982), Spectrum estimation and harmonic analysis, *Proc. IEEE*, *70*, 1055–1096.

Tivey, M. K., A. M. Bradley, T. M. Joyce, and D. Kadko (2002), Insights into tide-related variability at seafloor hydrothermal vents from time-series temperature measurements, *Earth Planet. Sci. Lett.*, *202*, 693–707.

Tomic, J., R. E. Abercrombie, and A. F. do Nascimento (2009), Source parameters and rupture velocity of small M ≤ 2.1 reservoir induced earthquakes, *Geophys. J. Int.*, *179*, 1013–1023, doi:10.1111/j.1365-246X.2009.04233.x.

Van Ark, E., R. S. Detrick, J. P. Canales, S. M. Carbotte, A. J. Harding, G. M. Kent, M. R. Nedimovic, W. S. D. Wilcock, J. B. Diebold, and J. M. Babcock (2007), Seismic structure of the Endeavour Segment, Juan de Fuca Ridge: Correlations with seismicity and hydrothermal activity, *J. Geophys. Res.*, *112*, B02401, doi:10.1029/2005JB004210.

Van Dover, C. L. (2000), *The Ecology of Deep-Sea Hydrothermal Vents*, Princeton Univ. Press, Princeton, N. J.

Von Damm, K. L., A. M. Bray, L. G. Buttermore, and S. E. Oosting (1998), The geochemical controls on vent fluids from the Lucky Strike vent field, Mid-Atlantic Ridge, *Earth Planet. Sci. Lett.*, *160*, 521–536.

Wilcock, W. S. D. (1998), Cellular convection models of mid-ocean ridge hydrothermal circulation and the temperatures of black smoker fluids, *J. Geophys. Res.*, *103*, 2585–2596.

Wilcock, W. S. D., and A. McNabb (1996), Estimates of crustal permeability on the Endeavour segment of the Juan de Fuca mid-ocean ridge, *Earth Planet. Sci. Lett.*, *138*, 83–91.